Experimental and modeling studies of pattern growth and pattern invasion in heterogenous reaction-diffusion systems

A Dissertation

Presented to

The Faculty of the Graduate School of Arts and Sciences

Brandeis University

Department of Chemistry

Irving R. Epstein, Advisor

In Partial Fulfillment

of the Requirements for the Degree

Doctor of Philosophy

by

Delora K. Gaskins

May 2018

The signed version of this form is on file in the Graduate School of Arts and Sciences.

This dissertation, directed and approved by Delora K. Gaskins's committee, has been accepted and approved by the Graduate Faculty of Brandeis University in partial fulfillment of the requirements for the degree of:

DOCTOR OF PHILOSOPHY

Eric Chasalow, Dean of Arts and Sciences

Dissertation Committee:

Irving R. Epstein, Chair

Bing Xu

Enrique Peacock-Lopez

To my family and family-friends who have been my support during my time at Brandeis.

Thank you for being here (and there) for me. It wouldn't have been possible without you.

Acknowledgments

First, I would like to acknowledge Irv who took me into his group: first as an REU student and then again for my graduate program. He listened, gave advice, and helped me grow organically as a graduate student as a member of this community. Also, I would like to acknowledge Milos who let me play around downstairs and was an excellent mentor for an experimentalist and human being.

I'm grateful for the wonderful people I met through Posse. I couldn't have asked for a better mentor of mentors than Melissa. Kim also was there for me. Cara, for our weekly hangouts while our Posses were babies. My posse BSP5 (Ama, Brian, Diana, Emilia, Genesis, Joel, Rabab, Rashieda, MacRegga, Steven) aka the best posse, you are my family.

My roomies Annie, Leanna, Jackie, and bonus roomies Charles and Tom. Thank you for being the humans you are ... Mathieu, thank you too for your companionship. Brizzles, always! You are loyal and smart and brave and kind and I'm so glad that you came from the air and formed my home here. My school friends, Tina and Ali and Zack Attack and Justin who kept my birth home not too far away.

My extended family, especially the Robbins and McCann families. I love you and am so grateful to have gotten to know you better. My parents who have supported me throughout my career. My brother David and sister Alisea as we've grown closer even though we've technically never lived so far apart. Momma Bear Theresa as well.

My science family who keeps getting bigger the longer I stay in science. My undergrad labmates Kim, Edsel, and Tim and Steve, my undergrad advisor. My labmates here Tamás and VH, ZAJA, Domenico, Naziru, Chris, Vinh, Raphael, Sridar and Revs (by adoption). My undergrads Emily and Jamie and Josephine, I learned a lot as your mentor. The multitude of undergrads in our group, especially my collaborator Sam. Şölen for the kahve and Achini also. The biologist triad including Kene, KC, and Cara and the physicists Jan and Sonja and Nate. Also, my sister-in-science Itana.

Abstract

Experimental and modeling studies of pattern growth and pattern invasion in heterogenous reaction-diffusion systems

A dissertation presented to the Faculty of
the Graduate School of Arts and Sciences of
Brandeis University, Waltham, Massachusetts

by Delora K. Gaskins

Experimental studies of pattern formation are carried out in the aqueous chlorine dioxide-iodine-malonic acid (CDIMA) oscillating chemical reaction in an open configuration and in the reverse microemulsion Belousov-Zhabotinsky-Aerosol OT (BZ-AOT) oscillating chemical reaction in a closed configuration. These systems form patterns in space and time because of the wave, Turing, and Hopf instabilities.

In the first system, the addition of the halides bromide and chloride changes the wavelength of the Turing patterns by up to five times the natural wavelength of the pattern. This result has significance because the largest previous increase was no more than a factor of two and was unable to be achieved within a single experiment. These changes were able to be qualitatively reproduced with a realistic chemical model.

In the second system, multiple invasion (Turing invading bulk oscillations) styles were observed. In addition, a modulated standing wave pattern was observed to invade a bulk oscillation domain. This pattern in turn was replaced as spirals were formed. This "death" by spiral formation was qualitatively reproduced using a chemical toy model.

Additionally, patterns were observed when the BZ-AOT system (bubble-free, and non-bubble free) was incorporated into a membrane. A microemulsion-based organogel that is stable in the reacting BZ-AOTmedium was also synthesized. These are significant steps towards the building of a reactor for the BZ-AOT reverse microemulsion system.

Contents

List of Figures

List of Tables

Chapter 1

Introduction

1.1   Hopf, Turing, and wave instabilities

Interactions and reactions are at the heart of chemistry. Chemists often focus on the equilibrium state, where the reactants and products have settled to fixed concentrations, but the dynamics of far-from-equilibrium chemical systems can be non-trivial in both space and in time. Reactions proceed to equilibrium unless their far-from-equilibrium state is maintained through a source of energy, for example in the form of a feed of unreacted reagents. This input of energy allows for non-equilibrium steady states to be maintained. These non-equilibrium steady states have fixed concentrations of reagents over time, but have concentration values distinct from the equilibrium state. When this input of energy occurs the system is no longer a closed system (batch system) but an open one. The experimental systems in this thesis use both batch and open, continuously fed reactor designs in the study of far-from-equilibrium pattern formation.

We are interested in the dynamical behavior of chemical systems (how the chemicals which exist in space change over time). There are a number of disciplines that study dynamical

systems, and over time a language and mathematical framework have been developed for describing dynamical features that occur and the instabilities that can give rise to them. The simplest type of behavior in a dynamical system is when all of the variables have a fixed value in time. These "fixed points" in chemical systems are the steady states we are familiar with in chemistry.

Oscillation is another fairly intuitive dynamical behavior. But it is rare in chemical systems; only a few families of chemical reactions are known to be capable of exhibiting this type of temporal dynamics. Oscillations in chemical systems are not like pendulums in physics. Chemical oscillators do not oscillate about their equilibrium point. Rather, the concentrations of intermediate species oscillate as the reactants are consumed and final products are produced.

The experimental chemical oscillators that have been discovered rely on activation-inhibition feedback loops through coupling and autocatalysis. An autocatalytic species in a chemical reaction promotes its own formation; an increase in this species increases the rate of formation of the species. Reaction 1.1 gives the simplest abstracted form of an autocatalytic reaction. In this case species X is autocatalytic.

$$A + X \longrightarrow 2\,X \tag{1.1}$$

Autocatalytic reactions themselves are rarely if ever the result of a single elementary step reaction, but rather the summation of elementary steps, e.g., (Reactions 1.2 and 1.3).

$$A + X \longrightarrow Y \tag{1.2}$$

$$Y \longrightarrow 2\,X \tag{1.3}$$
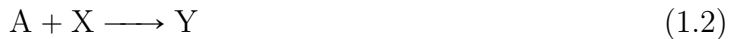
A species that is autocatalytic is called an activator. An inhibitor species reduces the amount of the activator species. The feedback is due to species being present in multiple steps of the chemical mechanism, which couples the differential equations that result from the rate laws of the steps of the reaction mechanism. In the remainder of this section, we will walk our way through the Hopf bifurcation, responsible for the oscillations we see in the experiments in this thesis, but in a simplified chemical model called the Brusselator. We'll start by thinking about the reactions in a mathematical framework. Reactions have the form of Eq. 1.4 where the capital letters are reagents and the small letters are the stoichiometric coefficients. If the reaction (step) is an elementary reaction (step), the corresponding rate law is 1.5. Not all chemical models are composed of elementary steps, and the rate laws for non-elementary steps must be determined empirically. The chemical concentrations of A and B are indicated by [A] and [B]. In other disciplines, the notation C_A or A can be used to indicate the concentration of species A. The forward rate constant k_f is constant for constant temperature and ionic strength.

$$aA + bB \longrightarrow cC + dD \tag{1.4}$$

$$\text{Reaction Rate} = k_f[A]^a[B]^b \tag{1.5}$$

One can utilize calculus and the rate laws for the steps of a mechanism to determine how the concentration of an individual species varies as a function of time in the rate equations. These equations give how the individual reactants change or evolve over time, and in dynamical systems language are called evolution equations.

The Brusselator, below, is the first chemically realistic toy model to exhibit oscillations.

It does so via the Hopf bifurcation.

$$A \longrightarrow X \tag{1.6}$$

$$B + X \longrightarrow Y + D \tag{1.7}$$

$$2\,X + Y \longrightarrow 3\,X \tag{1.8}$$

$$X \longrightarrow E \tag{1.9}$$

The autocatalytic step here is 1.8, and it is autocatalytic in the species X. The assumption in this model is that all of the steps are elementary steps, which we know is slightly unphysical with step 1.8. The full set of evolution equations are as follows.

$$\frac{dA}{dt} = -k_1[A] \tag{1.10}$$

$$\frac{dB}{dt} = -k_2[B][X] \tag{1.11}$$

$$\frac{dX}{dt} = k_1 A + k_2[B][X] + k_3[X]^2[Y] - k_4[X] \tag{1.12}$$

$$\frac{dY}{dt} = k_2[B][X] - k_3[X]^2[Y] \tag{1.13}$$

$$\frac{dE}{dt} = k_4[X] \tag{1.14}$$

Making pool chemical approximations for A and B, where the concentration of these reactants is assumed to be much greater than the concentrations of the intermediates and products, and ignoring the species E, which grows monotonically, reduces the number of equations. By nondimensionalizing the resulting evolution equations, the following evolution equations can be obtained for X and Y. In these equations the concentrations of the variables and the time have been rescaled.

$$\frac{dX}{dt} = A + X^2 Y - BX - X \tag{1.15}$$

4

$$\frac{dY}{dt} = BX - X^2Y \tag{1.16}$$

To start to examine the dynamics of this model, we should find the simplest feature (the steady state(s)) by setting the derivatives with respect to time to zero. This system is at its steady state when $X = A$ and $Y = B/A$ (derivation in Appendix A.1). This steady state can be stable or unstable. The difference lies in how small concentration changes from the steady state evolve in time. If the steady state is stable, there is a region about the steady state where all concentrations of the system will go to the steady state over time. So, if the system has small perturbations which push it to other nearby concentration values, then it will relax to the stable steady state. Figure 1.1 (left) shows the evolution of the system when the system is set to the stable steady state and then given a small random perturbation. The system evolves back to the steady state concentrations.

For the simulation in Figure 1.1 (right), the parameter B has been changed so that the steady state is no longer stable. This means that if the initial condition of the system is the steady state and it is perturbed then X and Y will evolve further from their steady state values.

We can understand this through the theory of bifurcations. Control parameters are parameters of the system that can be varied. In this system, A and B are control parameters. When a system undergoes a qualitative change in behavior as a result of changing of a control parameter, it undergoes a bifurcation. So in this example, B is the control parameter of interest. The bifurcation that occurs in going from Fig. 1.1 (left) to Fig. 1.1 (right) is the Hopf bifurcation.

The **Hopf bifurcation** (supercritical) occurs in ordinary differential equations when a fixed point loses stability and a stable limit cycle appears. The path in phase space that starts at some set of initial conditions at time t and develops as the reaction progresses is
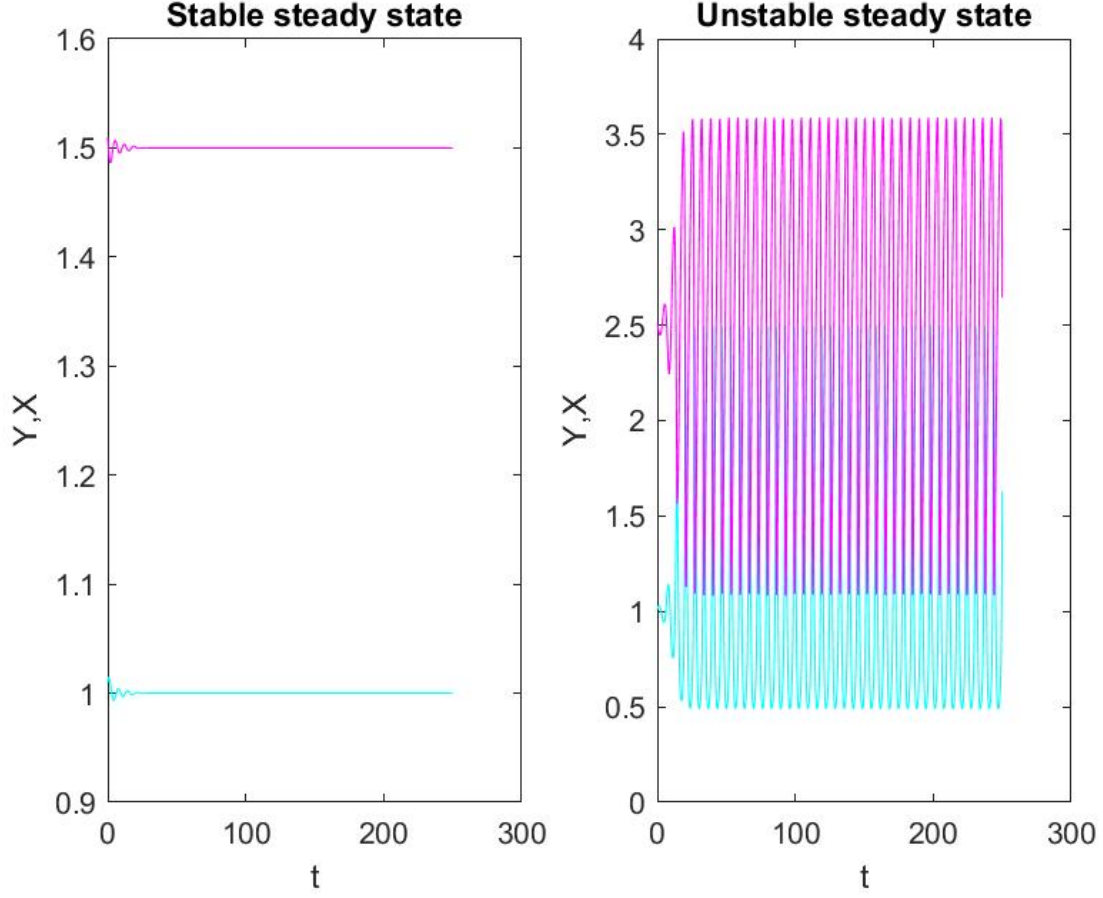
Figure 1.1: Dynamics of the Brusselator with B such that the steady state is stable (left) and B such that the steady state is unstable (right). Parameters and initial conditions are as follows: (left) $A = 1, B = 1.5, X_0 = 1.0096, Y_0 = 1.5096$ (right), $A = 1, B = 2.5, X_0 = 1.0096, Y_0 = 2.5096$

called the trajectory of those conditions. A limit cycle is a trajectory in the system which is an isolated, closed curve. For a chemical model with a limit cycle, the concentrations of the species oscillate through one period for each trip around the limit cycle.

Fig. 1.2 shows two trajectories that are attracted to the limit cycle. The initial condition for each of these trajectories is marked with a red dot. The trajectory starts at the initial condition and moves in concentration space as the reaction progresses. One trajectory begins from a small perturbation from the steady state (left) and the other (right) is started outside of the limit cycle.

We have spent most of the introduction so far with the Brusselator to approach the fundamental understanding of the Hopf bifurcation which generates oscillations. These oscillations happen in time at a single point in space. Real chemical systems are three dimensional of course. When the transport of reagents occurs through Fickian diffusion exclusively, we have a reaction-diffusion system. When there is no gradient, that is, due to perfect mixing each point has the same concentration, we can ignore the last term in the reaction-diffusion equations 1.17 and 1.18, where D_X and D_Y are the scaled diffusion coefficients of species X and Y. This reduces the partial differential equations to the ordinary ones. 1.15 and 1.16.

$$\frac{dX}{dt} = A + X^2Y - BX - X + D_X\nabla^2 X \tag{1.17}$$

$$\frac{dY}{dt} = BX - X^2Y + D_Y\nabla^2 Y \tag{1.18}$$

To look at the instabilities of this model near their onset, we can use linear stability analysis to generate the dispersion curve. In these diagrams, the independent variable is the wavenumber of the perturbation with wavenumber (k). The dependent variables are the eigenvalues (σ_k) determined from the characteristic polynomial. If the eigenvalues have a positive real part at k, then perturbations at this spatial frequency will grow and there is
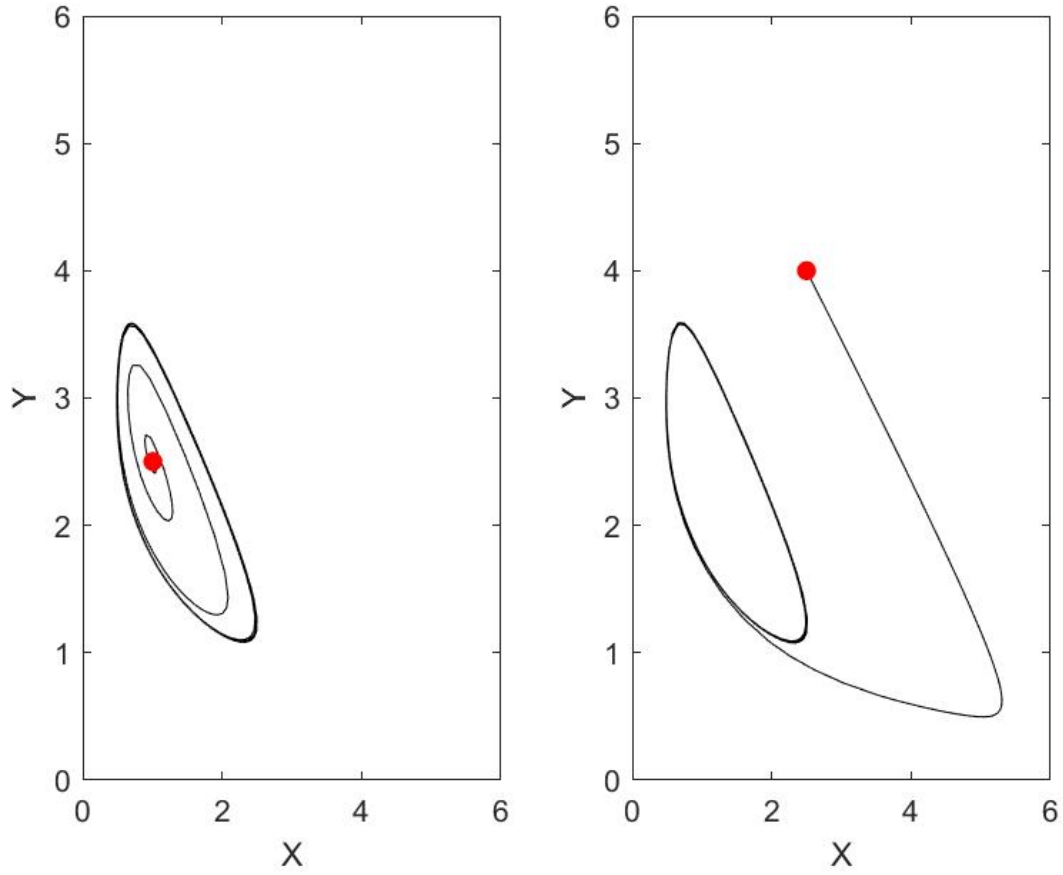
Figure 1.2: The limit cycle of the Brusselator is approached from near the steady state (left, $X_0 = 1.0027, Y_0 = 2.5067$) and from the outside (right, $X_0 = 2.5, Y_0 = 4$). The initial conditions are indicated by the red dot

an instability. The onset of the bifurcation occurs when the sign switches from negative to positive. If the imaginary part is zero then the pattern of the system is stationary in time, and if both the imaginary and real part of the eigenvalues are non-zero, then the patterning of system oscillates in time.

When the wavenumber is zero, the perturbation is uniform in space, so that if the system oscillates in time, then it is a bulk oscillation. The sign of the real part of eigenvalues changes when $B = 1 + A^2$ (Appendix A.2). This is B_{onset} for the Hopf bifurcation. Figure 1.3 shows the onset of the Hopf bifurcation in the spatially-extended Brusselator. The parameter B is the bifurcation parameter here with the other parameters fixed, and it is increased from $0.7 * B_{onset}$ (top) to B_{onset} (middle) to $1.3 * B_{onset}$(bottom) where B_{onset} is 10 (A=3, so $B = 1 + 3^2$). The line $Re(\sigma_{k2})$ crosses $\sigma_k = 0$ at $k = 0$ in the middle plot of the figure.

The **Turing instability** is not possible in the system of equations 1.15 and 1.16 because of the absence of diffusion terms. Figure 1.4 shows the onset of the Turing instability in the spatially-extended Brusselator. The onset of this instability occurs when the real part of the eigenvalues is positive while the imaginary part is zero.

The parameter B is the bifurcation parameter, Appendix A.2 shows the derivation for B_{onset} which is $(1 + A * (D_x/D_y)^{.5})^2$. The figure 1.4 shows the dispersion curves as b is increased from $0.8 * B_{onset}$ (top) to B_{onset} (middle) to $1.2 * B_{onset}$(bottom) where B_{onset} is $5.45(\sigma_k)$. The line $Re(\sigma_{k1})$ crosses $\sigma_k = 0$ in the middle plot of the figure. It does so while $Im(\sigma_{k1}) = Im(\sigma_{k2}) = 0$. So these patterns are stationary in time. All of the perturbations at spatial frequencies with positive real eigenvalues will grow, but the one with the most positive eigenvalue will grow the fastest and dominate the system's behavior. This gives the pattern's characteristic wavelength.

The pure Hopf and pure Turing bifurcations give rise to bulk oscillations that are periodic in time but not in space and patterns that are periodic in space and stationary in time,
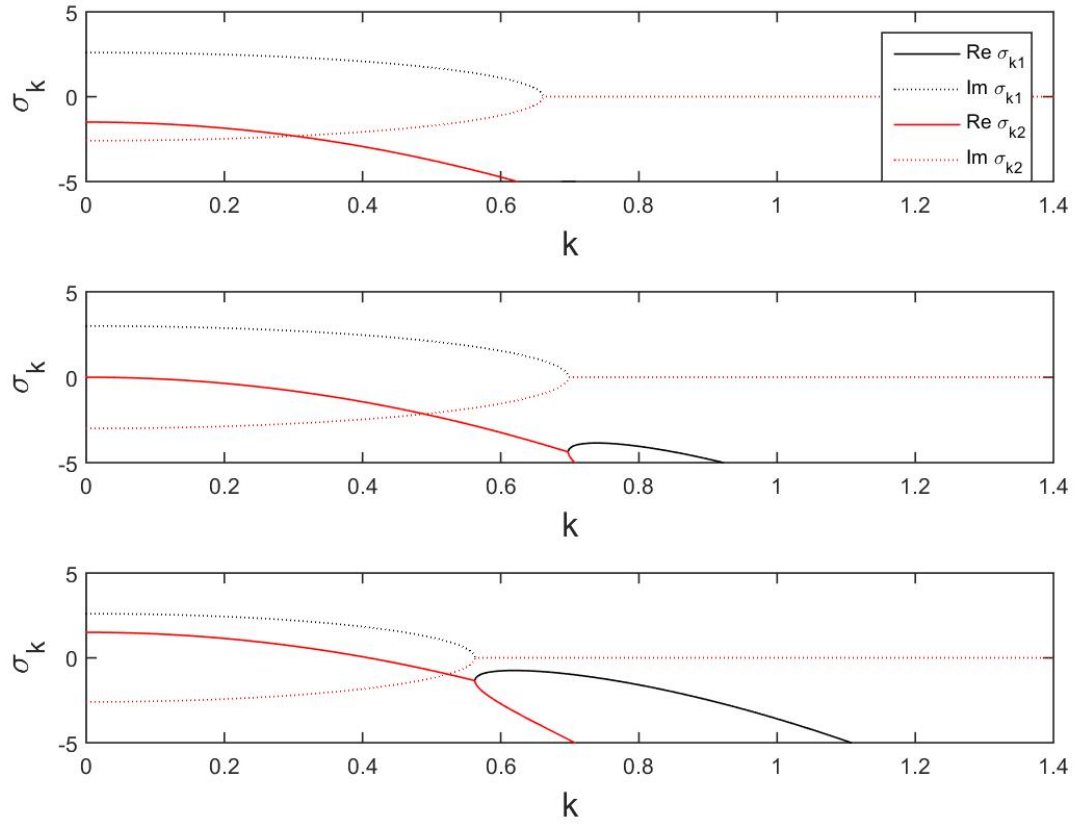
Figure 1.3: Hopf bifurcation $A = 3, D_X = 8, D_Y = 10, B = 7$(top), 10, (middle), 13(bottom)
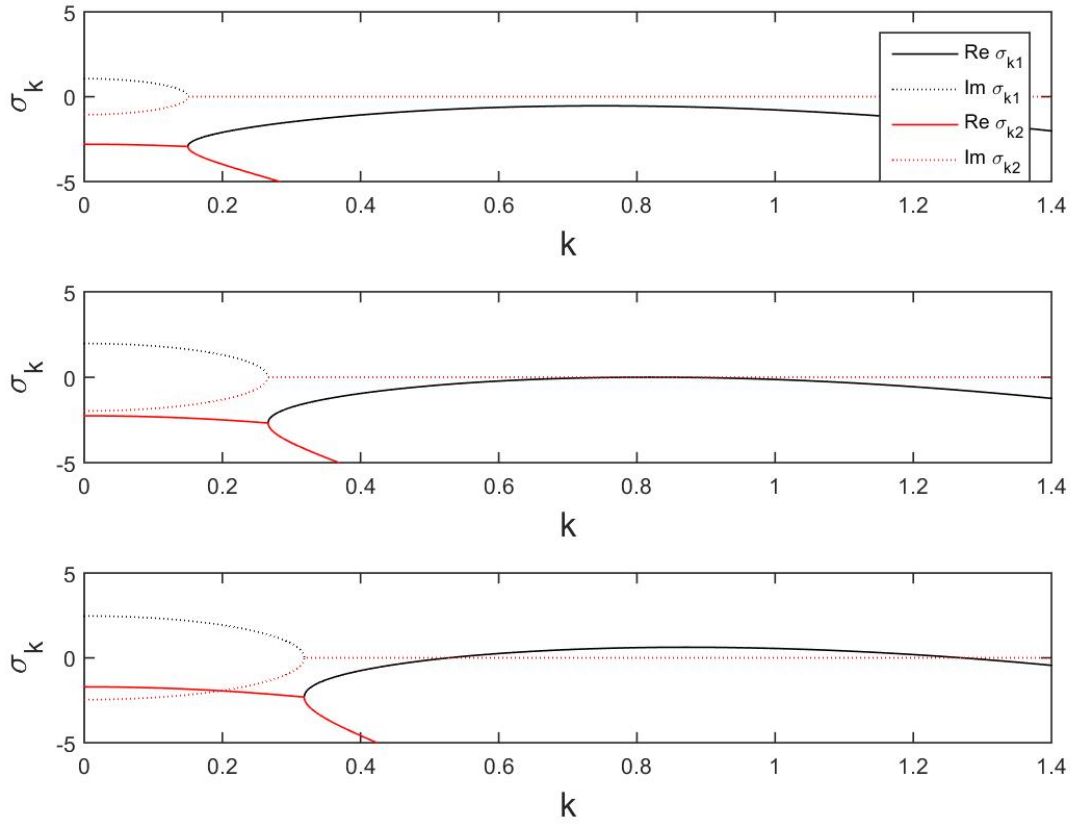
Figure 1.4: Turing bifurcation $A = 3, D_X = 8, D_Y = 10, B =$4.38(top) 5.48(middle) 6.57(bottom)

respectively. Chapter 3 of this thesis focuses on Turing patterns, using the concentration of added halides as a bifurcation parameter to produce multifold increases in the characteristic wavelength of the patterns in the chlorine dioxide-iodine-malonic acid (CDIMA) system.

Chapter 4 focuses on the interaction of the two instabilities, Turing and Hopf, in the Belousov-Zhabotinsky (BZ)-Aerosol OT reverse microemulsion. The codimension two point of this system is where the onset of the Turing instability and the Hopf bifurcation occur at the same value of the bifurcation parameter. At regions in parameter space beyond the onset of both of these instabilities, patterns can form with a Turing and a Hopf mode. This means that the patterns can be periodic in both space and time.

In the Brusselator, a two variable model, the interaction of the Turing and Hopf instabilities is the only way to obtain patterns that are periodic in space and periodic in time. The **wave instability** is a single instability, but requires a minimum of three variables, and it can generate patterns that are periodic in space and periodic in time [8]. Chapter 5 focuses on patterns that are periodic in space and time: standing waves in the Belousov-Zhabotinsky-Aerosol OT (BZ-AOT) system.

The Brusselator is a good model to illustrate the Turing and Hopf instabilities, but we now turn to the chemical systems where Turing patterns, bulk oscillations, waves and more complicated spatio-temporal phenomena arise.

1.2 BZ and CDIMA, aqueous chemical oscillators

1.2.1 Belousov-Zhabotinsky reaction

There are lessons to learn from the story of the acceptance/non acceptance of the Belousov-Zhabotinsky (BZ) oscillating chemical reaction by the greater chemical community. Despite

the publication of the Bray reaction [9] roughly forty years earlier, and the existence of other chemical oscillators, Boris Belousov found it difficult to publish his discovery of pale yellow to colorless oscillations that he found while searching for an inorganic analog of the citric acid cycle. Belousov's reaction mixture was composed of citric acid, which functioned as an organic substrate, cerium as a catalyst, sodium bromate and sulfuric acid. His initial studies included the observation that the oscillation frequency increases with increasing temperature. His reviewers rejected the manuscript on the grounds that oscillations in a closed system could not happen. But what this reaction showed was the fundamental misunderstandings of the second law that the community had and its unwillingness to try to reproduce a phenomenon. He eventually published his discovery in a booklet of his own institute: *A Collection of Short Papers on Radiation Medicine* [10].

Anatol Zhabotinsky took up work with Belousov's recipe; the two corresponded but never ultimately met [11] and Zhabotinsky made the first steps into determining the reaction mechanism. It took another twenty years for the development of a plausible full mechanism that could explain the oscillation and this was done by Field, Körös, and Noyes. [1].

This reaction is one member of the bromate family of oscillators. The chlorine dioxide-iodine-malonic acid (CDIMA) reaction is part of the chlorite family [2], and this family also includes the chlorite-iodide-malonic acid reaction and the chlorite-iodide reaction. The schemes of the core oscillators of these reactions are shown in figure 1.5.
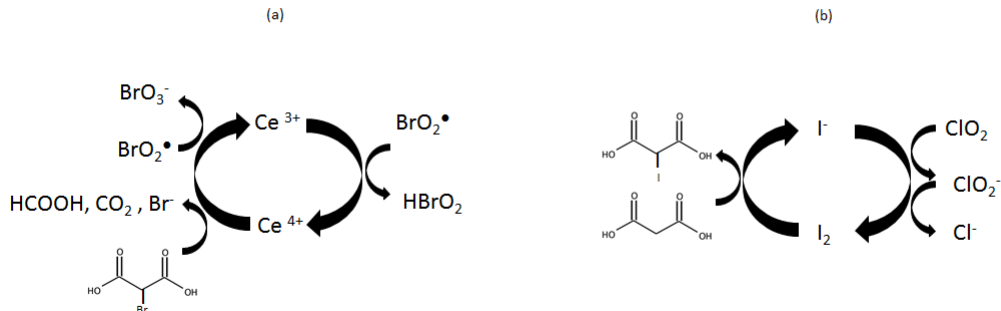
Figure 1.5: Depictions of oscillatory chemical reactions (a) BZ [1] and (b) CDIMA [2]

1.3 Chemical oscillators in heterogeneous media, including BZ-AOT

The previous section introduced the aqueous chemical oscillators of CDIMA and BZ. The two oscillators that we use in this thesis are CDIMA and the BZ reaction incorporated into a reverse micellar solution that will be outlined in section 1.3.2. This is one of the ways that chemical oscillators can be incorporated into heterogeneous media. Table 1.1 outlines examples in the literature of CIMA/CDIMA and BZ oscillators in heterogeneous media.

	Chemical Oscillators		
	CIMA/CDIMA	BZ	
Phase of chemical oscillator	aqueous	aqueous	reverse microemulsion
Inert gel/polymer matrix	-first observed Turing patterns [12] -Turing pattern wavelength [14]	agar gels[13]	membranes in section 7.1
surfactant added	DTAB[15]	-BZ AOT [16]	
non-inert gel	alkylammonium gel[15]	BZ beads [17] Chemoresponsive gels[18]	
short polymer		PEG + BZ [19]	PEO + BZ AOT [20]

Table 1.1: Chemical Oscillators in Heterogenous Media

1.3.1 Inert Gels/Matrix

An inert porous matrix can be used as a medium to stabilize pattern formation in an open reactor configuration. Patrick De Kepper's group in Bordeaux was studying the oscillations in an open CIMA system when they observed the formation of a stationary pattern and recognized that it was a Turing pattern [12]. These patterns were visualized with starch, which complexes with triiode to form a dark purple color and slows the effective diffusion of the inhibitor iodide, which was necessary for the pattern formation. This was the first experimental observation of a Turing pattern and CIMA/CDIMA became the prototypical system for the observation of Turing patterns in chemical systems.

By changing the percent composition and identity of the gels which composed the inert gel matrix, the Swinney group showed the dependence of the pattern wavelength on the effective diffusion of the reacting species[14]. Gels have also been used to stabilize the BZ reaction against advection. Millipore membranes were initially used to visualize the three dimensional patterns in the reaction [21] with a recipe which used ferroin as a catalyst for better contrast with the ferriin (oxidized state) being blue and the ferroin (reduced state) being red. Interest in a transparent medium led to the use of gels such as agar as a medium for the reaction [13].

1.3.2 BZ-AOT

Aerosol OT is a surfactant (**surf**ace **act**ive age**nt**) and its structure is shown in figure 1.6 (a). In ternary mixtures of this surfacant, reverse micellar structures may form. The ternary diagram in Figure 1.6 shows the region of stability for this type of self organization as well as the liquid crystal domain [3].

Figure 1.7 depicts the structure of a surfactant, with a hydrophillic head group and
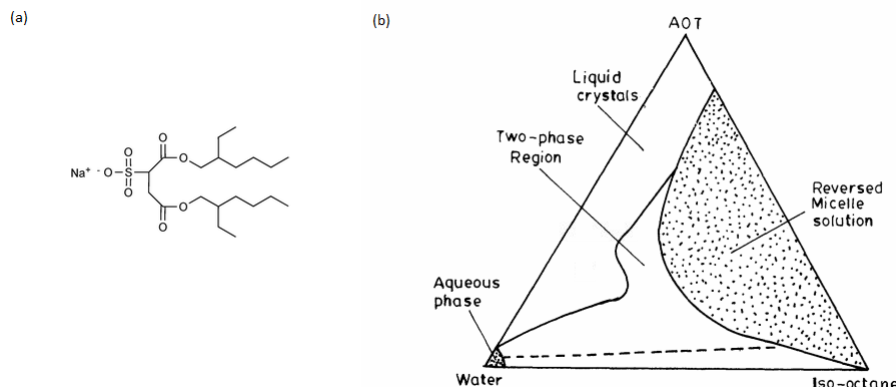
Figure 1.6: (a) S tructure of Aerosol OT (b) ternary diagram of oil, water, and AOT[3]

hydrophobic tail group. In an oil-in-water microemulsion the tail is oriented into the micelles containing oil. In a water in oil microemulsion (termed reverse microemulsion) the tail is oriented outward in the continous oil medium. The incorporation of the aqueous BZ chemical oscillator into the droplets in an Aerosol OT reverse microemulsion created a rich, new patterning forming system. Initial investigations found oscilliations in the well stirred system [22, 23, 24] and in a spatially extended system many novel patterns were found including antispirals [25], jumping waves [26], and accelerating waves[27].

PEG, a short polymer, has been added to BZ-AOT and observed to lengthen the duration of pattern formation. This is proposed to be because it holds groups of water droplets together over the course of reaction [20]. This is different than the way the short polymer affects the BZ reaction, in changing the patterns that are formed. It would be of interest to create an inert medium for the BZ-AOT reaction to create an open system. Preliminary results on the BZ-AOT reaction in an inert polyvinylidene difluoride $(CH_2CF_2)_n$)membrane are shown in section 7.1. Additionally, initial work with reverse microemulsion based organogels is discussed.

Surfactant

Counterion, for
ionic surfactants

Hydrophilic
head group

Hydrophobic tail

**Micelles in
Microemulsion**

Water

**Reverse Micelles in
Reverse Microemulsion**

Oil
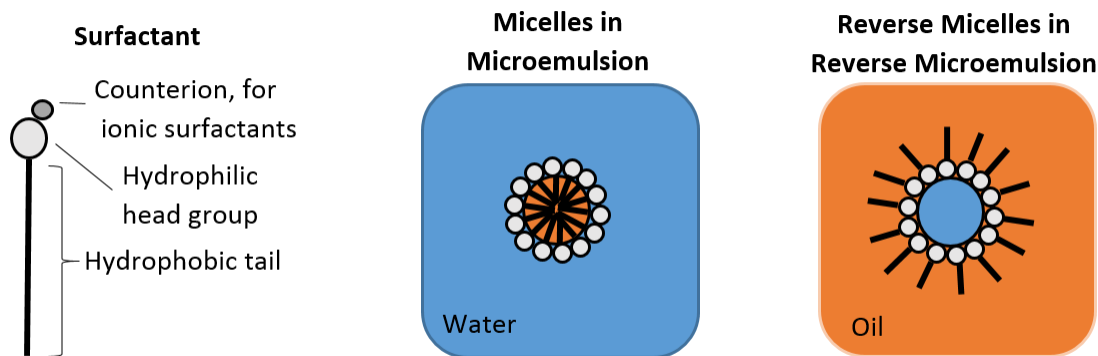
Figure 1.7: Structure of a surfactant, and how it forms a micelle in a microemulsion and a reverse micelle in a reverse microemulsion.

1.3.3 Non-inert gels

If the gel has a reactive pendant or immobilizes a reagent in the reaction then it is no longer inert. In the case of the BZ, it is typically the catalyst that is immobilized[28][17]. If the the swelling/deswelling of the gel can be coupled to the oxidation state of a pendant catalyst then the gel can oscillate [18] which is a novel but somewhat difficult to harness application.

Because of the high molecular weight of starch, it can take several hours to diffuse to give enough contrast in the CDIMA reaction in an inert gel. A gel with an alkyl ammonium group was synthesized and was also able to generate Turing patterns with sufficient contrast. The alkyl ammonium moiety was able to slow down the effective diffusion of iodide as with starch [15].

Chapter 2

Methods

The experimental systems that generate patterns in this thesis are the CDIMA reaction in an open configuration and the BZ-AOT reaction in a batch reactor. This chapter includes a discussion on the variations of BZ/BZ-AOT, outlines the preparation of the reagents for both reactions, and how they were used in their respective batch and open conditions.

The recipes for the BZ-AOT patterns are slightly different for each of the patterns observed. With BZ, one varies the concentrations or identities of the substrate of bromination or the catalyst. The original substrate was citric acid (Figure 2.1(a)) but today the reaction is typically done with malonic acid (Figure 2.1(b)). Malonic acid and bromomalonic acid decarboxylate, so a substrate which does not, like 1,4 -cyclohexanedione (Fig.2.1(c)), can be used to replace it. Bubble formation can be a problem, as CO_2 bubbles formed take up space, altering the reacting volume for fixed volume reactors and also potentially displace patterning. This becomes more of a problem at high acidities and temperatures because of the more rapid kinetics of reaction. In section 7.1, we report our results in substituting cyclohexadione in the BZ reaction incorporated in an Aerosol AOT reverse microemulsion.

In addition to changing the substrate, the catalyst ferroin (Fig.2.2 (b)) can be replaced.
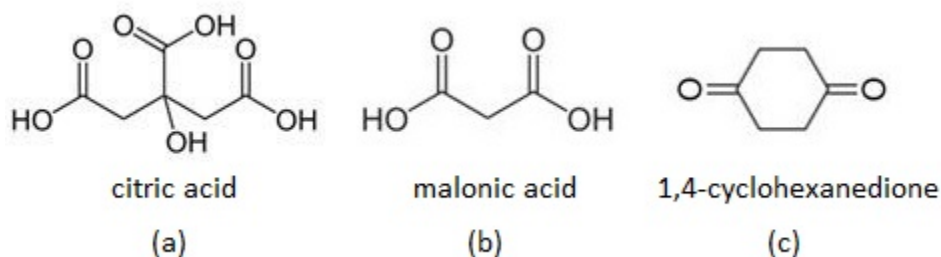
Figure 2.1: Substrates of the Belousov-Zhabotinsky reaction
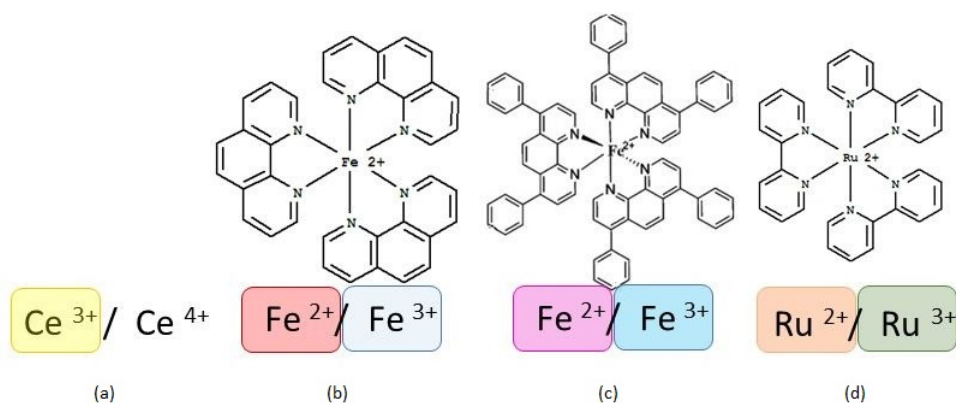
Figure 2.2: Catalysts of the Belousov-Zhabotinsky reaction

Bathoferroin, which is more pink than ferroin due to its additional benzyl moieties, can also be used (Fig.2.2 (c)). Ruthenium bipyridine (Fig.2.2 (d)) is photosenstive and therefore can be useful for perturbing the reacting system.

Here we will explain in further detail about the nature of the BZ-AOT emulsion. Indirect measurement methods for the radii of droplets include dynamic light scattering and NMR. In dynamic light scattering, the measurements of the hydrodynamic radius are calculated from autocorrelation as the droplets diffuse, and can only be conducted with colorless solutions. BZ-AOT has a colored catalyst and so measurements with dynamic light scattering are done in the absence of catalyst.

Law and Britton showed with NMR that the radii of the individual droplets depend on the ratio of AOT molecules to water molecules (ω). In addition, they showed polydispersity and droplet radii depend on volume fraction ϕ_d, which is the volume of the dispersed phase (water and AOT) over the total volume of the system [29] . Increasing the ϕ_d effectively increases the concentration of droplets until the percolation threshold, where channels form. If time is allowed to elapse after sample preparation, the solutions become monodisperse, as was shown both by Law and by Carballido [20]. Carballido et al. also found that the addition of polyethyleneoxide increases the lifetime of the polydispersity.

The wave patterns form at higher acidities than the Turing patterns do in this thesis. This is consistent with prior work on this system in that modifications that lead to increased reaction rates (temperature [30], polymer addition [31], ω [32]) increase oscillation frequency, decrease Turing pattern wavelength, and lead to a transition of Turing patterns to waves.

2.1 Solutions preparation

2.1.1 Chlorine dioxide-iodine-malonic acid reaction

Solutions were prepared to give concentrations of $I_2 = 0.35$ mM, [MA]= 1 mM, $ClO_2 = 0.1$ mM, [poly(vinyl alcohol)] = 10 g L^{-1}, and [H_2SO_4]=10 mM upon initial mixing in the reactor. Solutions were prepared as follows: I_2 was added along with H_2SO_4 and cosolvent acetic acid (10% v/v) and left to dissolve overnight. ClO_2 solution was prepared from stock that had been synthesized according to reference ([33]). These solutions were kept in darkness after preparation to minimize photodegredation, and their concentrations were checked spectrophotometrically before each experiment. The poly(vinyl alcohol) (PVA, Sigma-Aldrich, average molecular weight 9,000-10,000, 80% hydrolyzed) stock solutions and solutions of

NaBr and NaCl were prepared freshly each week, while fresh NaI solutions were prepared immediately before each reaction run.

2.1.2   Belousov-Zhabotinsky-Aerosol OT reaction

Standard preparation of BZ-AOT

All reagents were purchased from Sigma-Aldrich, except AOT, which was obtained from ACROS Fisher. Two different microemulsion stock solutions were prepared in order to prevent the BZ chemical species from reacting. The first microemulsion (MEI) contained malonic acid (MA), and sulfuric acid, and the second (MEII) contained bromate and ferroin. MEI and MEII contained equal amounts of 1.5 M AOT in cyclooctane. Both MEI and MEII were stirred for approximately 45 min. The microemulsions MEI and MEII were then combined at a 1:1 ratio and cyclooctane was added to the resulting microemulsion to control the water droplet volume fraction ($\phi_d = $ [water]/[oil]). The time elapsed between combining MEI and MEII with cyclooctane and transferring the reacting microemulsion to the reactor was approximately 1 min. The concentrations of the BZ reactants for the aqueous phase of the reacting microemulsion were [MA] $= 0.25$ M, [H_2SO_4] $= 0.20$ M, [$NaBrO_3$] $= 0.20$ M, and [ferroin] $= 0.01$ M. The [water]:[AOT] ratio of the reacting microemulsion was $\omega = 12.347$, and the water droplet volume fraction was $\phi_d = 0.50$.

Bathoferroin preparation

In the case of the segmenting scroll rings pattern, the catalyst bathoferroin was prepared *insitu*. Bathoferroin is synthesized from $FeSO_4 \cdot 7\,H_2O$ and the bathophenathroline ligand. The bathophenantholine ligand is dissolved in the AOT/cyclotane for ME II, prior to the addition of freshly made solution of aqueous iron II sulfate and also the bromate solution.

2.1.3 CHD preparation

We prepared a bubble-free version of the BZ-AOT system using cyclohexanedione. In this variation, the measured amount of cyclohexanedione is added to MEI prior to mixing of the oil and water phase. This replaces the malonic acid of the standard BZ-AOT.

2.1.4 Solution conditions by pattern

Turing-Hopf rings (Section 3):

[MA] = 0.25 M, [H_2SO_4] = 0.40 M, [$NaBrO_3$] = 0.20 M, and [ferroin] = 0.01 M. ω = 11.11, ϕ_d = 0.46 and ω = 12.35, ϕ_d = 0.45

Invading Standing Waves (Section 5):

[MA] = 0.25 M, [H_2SO_4] = 0.40 M, [$NaBrO_3$] = 0.20 M, and [ferroin] = 0.01 M. ω = 11.11, ϕ_d = 0.46 and ω = 12.35, ϕ_d = 0.45

Segmented Scroll Rings (Section 6.1):

[MA] = 0.3 M, [H_2SO_4] = 0.2M, [$NaBrO_3$]= 0.18 M, [Bathoferroin]=5mM, ω = 13.89, ϕ_d = 0.45

Growing Rings and Settling Turing Circles (Section 6.2):

Figure 6.7: [MA] = 0.25 M, [H_2SO_4] = 0.2M, [$NaBrO_3$]= 0.2 M, [Bathoferroin]=10mM, ω = 12.34, ϕ_d = 0.299, non-typical solution age = 2hrs 54min

Figure 6.9: [MA] = 0.25 M [H_2SO_4] = 0.25M, [$NaBrO_3$]= 0.2 M [Bathoferroin]=10mM, ω = 12.34, ϕ_d = 0.40, non-typical solution age, 1hr 45 min

Figure 6.10: [MA] = 0.25 M, [H_2SO_4] = 0.24M, [$NaBrO_3$]= 0.2 M, [ferroin]=10mM, ω =

12.34, $\phi_d = 0.400$, non-typical solution age, 21hrs 51 min

Figure 6.6: [MA] = 0.25 M, [H$_2$SO$_4$] = 0.2M, [NaBrO$_3$]= 0.2 M, [ferroin]=10mM, $\omega = 12.34$, $\phi_d = 0.400$, non-typical solution age, 1hr 39 min

Cyclohexanedione (Section 7) Figure 7.3:

Chemical conditions: [CHD]=0.83 M, [H$_2$SO$_4$] = 0.2M, NaBrO$_3$= 0.08 M, [ferroin]=10mM, $\omega = 12.34$, $\phi_d = 0.58$

2.2 Organogel preparation

AOT in cyclooctane (15 % w/w AOT) and gelatin in water(36 % w/w gelatin) solutions are combined once heated to 50 $\circ C$ and then are stirred vigorously at that temperature. The solution is sonicated to minimize bubble formation as the gel forms.

The specific procedure for the gel in figure 7.4: Weigh out 1.69 g gelatin type A in a small beaker. Weigh out 0.89 g AOT in a small Erlenmeyer flask. Pipette 6 mL cycloctane in the Erlenmeyer flask. Once the sonicator water bath has reached a temperature of at least 50 $\circ C$, pipette 2.28 mL reagent-grade water to the weighed-out gelatin in a 30-mL beaker. Sonicate the gelatin solution and the AOT solution separately in sweep mode for 10 minutes. Subsequently, mix the two aforementioned solutions vigorously until the mixture is of homogeneous and gel-like consistency. Sonicate the gel mixture in degas mode for at least 45 minutes.

2.3   Experimental

2.3.1   Batch reactors

Quasi two dimensional

Quasi-2D experiments were carried out using two glass windows separated by a Teflon gasket of 0.09 mm thickness. The glass windows were contained in a sealed reactor body. Light was passed through the bottom of the reactor to allow images to be captured by a charge-coupled device (CCD) camera. Images were captured at one image per second.

It should be noted that when localized spots appeared prior to the screwing on of the reactor cap to the rest of the reactor body, the circular spots became elongated along one axis. A white LED was placed underneath the reactor to allow images of the transmitted light to be captured by a charge-coupled device (CCD) camera. The camera was fitted with a 532 nm bandpass filter. The concentration ratio of the oxidation states of the catalyst, ferroin (reduced, red) and ferriin (oxidized, blue), determines the color of the system. White in the images corresponds to the blue state, with the darkness of the image increasing with the concentration of the reduced state of the catalyst.

Three dimensional

We employed a cylindrical quartz capillary with an internal diameter of 0.5 mm for the 3D experiments [34]. This capillary was sealed and then submerged in an index-matching fluid (cyclooctane). For reconstruction purposes, the capillaries were rotated at 4.5 seconds/revolution. Images (over several rotations at each time point) were acquired using CCD cameras.

2.3.2   Open reactor

The patterns in this study were formed by the CDIMA reaction in the gel layer of a continuously fed unstirred tank reactor (CFUR) coupled with a continuously stirred tank reactor (CSTR) imaged by a CCD camera (PixeLINK).

Solutions were fed via syringe pumps (New Era Pump Systems, NE-1600 and Cole-Palmer) into the CSTR, where they were mixed with three magnetic stirbars rotating at 1000 RPM. The CSTR chamber volume was 2.0 mL, and the residence time was 160 s. Quasi-two-dimensional patterns formed in the gel layer of the CFUR, which was composed of 2% agarose (Sigma-Aldrich, low EEO) gel with thickness less than the wavelength of the smallest pattern (maximum thickness 0.45 mm). Two membranes separated the CFUR and CSTR: a supported Anopore membrane (Whatman, pore size 0.2 μm, thickness 0.10 mm) impregnated with agarose gel (typically 4%) and a nitrocellulose membrane (Whatman, pore size 0.45 μm, thickness 0.12 mm). These membranes prevented advection in and provided support for the gel layer; the nitrocellulose also provided contrast for imaging. The working area of the reactor had a diameter of 25 mm. A glass optical window allowed for imaging of the patterns. This combined CFUR/CSTR reactor was thermostated at 4 °C.

2.4   Image processing

2.4.1   Wavelength determination

To determine the wavelength, a local equalization filter is applied to the pattern; a 2D Fourier transform then is obtained for that image. Figure 2.3 illustrates the procedure from the Fourier transform. The averaged radial power ($\bar{P}$) is calculated by summing the intensity of the Fourier spectrum at a given radius and dividing by the number of points at that

radius. The radius of the peak with the largest $(\bar{P})$ is then converted from a wavenumber to a wavelength.
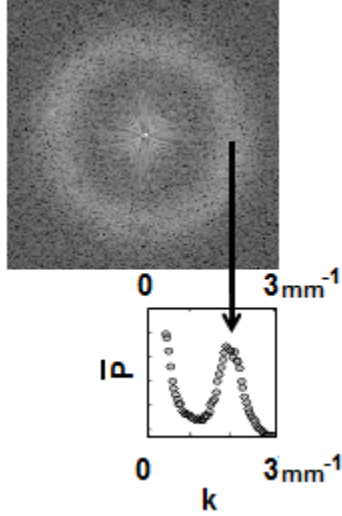
Figure 2.3: Method of determining wavelength from Fourier transform of CDIMA pattern. Averaged radial power$(\bar{P})$ is determined from the sum of Fourier intensity at a given radius divided by the number of points at that radius. The wavelength determined for this pattern is the reciprocal of the wavenumber of the peak indicated by the arrow.

2.4.2 Three dimensional reconstruction

The inverse Radon transform was used in MATLAB in order to tomographically reconstruct the three-dimensional capillary and the pattern from the two-dimensional projections over one rotation [34].

Chapter 3

Large Wavelength Turing Patterns

3.1 Introduction

There are several types of instabilities capable of generating patterns which were outlined in the introduction. This chapter focuses on the Turing instability. Again, the Turing instability gives rise to patterns through destabilization of a uniform steady state. Such Turing patterns are periodic in space and stationary in time and have a characteristic wavelength that is independent of the size of the system. The Turing instability has been used to explain pattern formation in a variety of biological and ecological systems, including patterns on butterflies and fish [35, 36, 37], mouse digit formation [38], and plant patterns in arid and semi-arid ecosystems [39, 40].

Changes in morphology and wavelength of a pattern in a system may indicate and lead to significant consequences for the system. In arid ecosystems, changes in pattern morphology and wavelength may serve as warning signs prior to desertification [41, 42]. Extinction of species through loss of habitat due to habitat fragmentation can arise when biomass patterns become less connected as a result of changes in pattern morphology and wavelength. Habitat

fragmentation has been argued to be one of the most important threats to global biodiversity [43, 44]. The evolutionary fitness of patterned animals such as guppies and zebras has been proposed to depend on the wavelength of the pattern on their skins [45, 46].

In this chapter, wavelength changes are induced in Turing patterns found in the chlorine dioxide-iodine-malonic acid (CDIMA) reaction [47]. The chlorinated species act as an inhibitor and the iodine-containing species serve as an activator in this system. The requisite difference between the diffusion coefficients of the activator and inhibitor for Turing patterns is achieved through complexation with an indicator, which slows the effective diffusion of the iodide species.

Prior work with these systems shows that the wavelength of the pattern is nearly independent of the feed concentration of the input reagents – with the exception of $[ClO_2]$. The wavelength of the pattern increases as the ClO_2 concentration is decreased [48]. Other factors that can alter the wavelength of the pattern by affecting diffusion include the identity and concentration of the complexing agent of the iodide [49] and the gel identity and density [14]. Slowing the rate at which a pattern can regrow at the edge of a steady state/pattern interface also allows for longer pattern wavelengths to be achieved [50]. The longest wavelength obtained through perturbation of CIMA/CDIMA to date in the literature is roughly 1.5 times the smallest wavelength. The experimental results in this chapter give unprecedented, multifold increases in wavelength. These results are supported with numerical simulations.

3.2 Results

Turing patterns began to appear spontaneously in the CFUR upon introduction of the ClO_2, I_2, and malonic acid solutions. The pattern morphologies were a mixture of spots and stripes with some honeycomb structures. Pattern wavelengths without halide addition were 0.51 ±
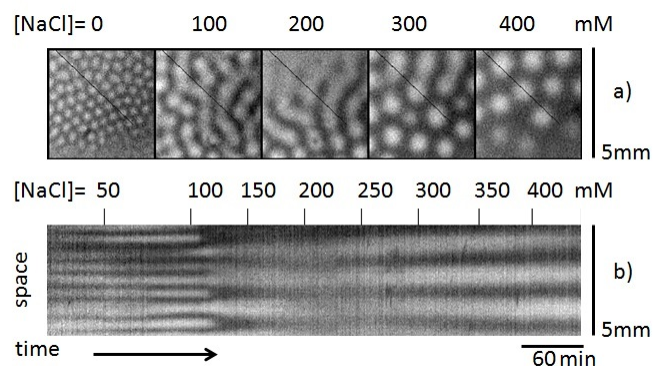
Figure 3.1: Response of Turing patterns in the CDIMA system to addition of NaCl. Light and dark regions correspond to low and high PVA-triiodide complex concentrations, respectively. a) Images showing response of initial pattern to concentrations of up to 400 mM NaCl. Image size is 5x5 mm. Slices from the black line in the figure are used to construct the space-time plot in b). b) Space-time plot (from the diagonal line in a)) shows how the pattern transitions as the NaCl concentration is increased.

0.05 mm as determined from the Fourier transform. The halide flow rate was changed to vary the halide concentration in the reactor, and a fixed total flow rate and constant residence time were maintained by varying the flow rate of a feed of 10 mM H_2SO_4. Halide concentrations were increased stepwise. We present our results for Turing patterns subjected to the addition of sodium salts of bromide, chloride, and iodide through the feedstock. Figures 3.1 and 3.2 show the response of the native Turing patterns to the addition of NaCl and NaBr. Different transitions – wavelength doubling for the NaCl additions and pattern disappearance and regrowth for the NaBr additions – were observed in the corresponding space-time plots. The focus of this chapter is the occurrence of large wavelength patterns. In contrast to the changes observed with the addition of NaCl and NaBr, addition of NaI had nearly negligible effect on the pattern. Only sub-mM concentrations of NaI could be added to the reactor before the pattern was lost and a uniform steady state became stable. Additions of NaBr gave a uniform state at a higher threshold and with NaCl at an even higher threshold, in accordance with periodic trends. NaBr also had a more pronounced effect on the wavelength
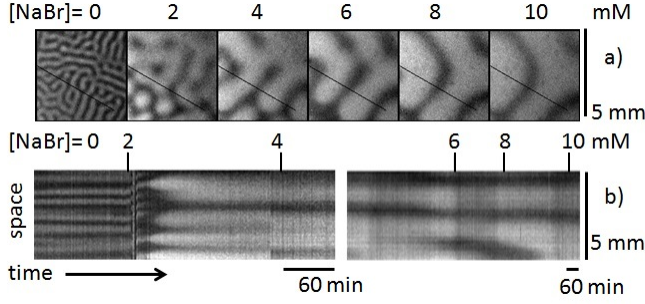
Figure 3.2: Response of Turing patterns in the CDIMA system to addition of NaBr. Light and dark regions correspond to low and high PVA-triiodide complex concentrations, respectively. a) Images showing response of initial pattern to concentrations of up to 10 mM NaBr. Image size is 5x5 mm. Slices from the black line in the figure are used to construct the space-time plot in b). b) Space-time plot (from the diagonal line in a)) shows how the pattern transitions as the NaBr concentration is increased.

than NaCl. Figure 3.3 shows the concentration ranges where NaCl, NaBr and NaI gave increases in pattern wavelength. Also shown in this figure are the largest patterns achieved by addition of each halide. We used the following two variable model to simulate large changes in the pattern wavelength.

$$\partial u/\partial \tau = \frac{1}{s}\left(a - u - \frac{4u}{1+u^2}v + \nabla^2 u\right) \tag{3.1}$$

$$\partial v/\partial \tau = b\left(u - \frac{u}{1+u^2}v\right) - cv + d\nabla^2 v \tag{3.2}$$

In this model, u is the dimensionless concentration of the activator species, iodide, and v is the dimensionless concentration of the inhibitor species, chlorite. The parameter s characterizes the triiodide-PVA complexation, and a and b are constants determined from the input concentrations of the reactants, which determine the kinetics of the reaction. The parameter d represents the ratio $\frac{D_{ClO_2^-}}{D_{I^-}}$.

The chlorite-iodide reaction step is first order in v and is accounted for in the third term of Eq. 3.1 and the second term of Eq. 3.2. We represent the chlorite-bromide and chlorite-
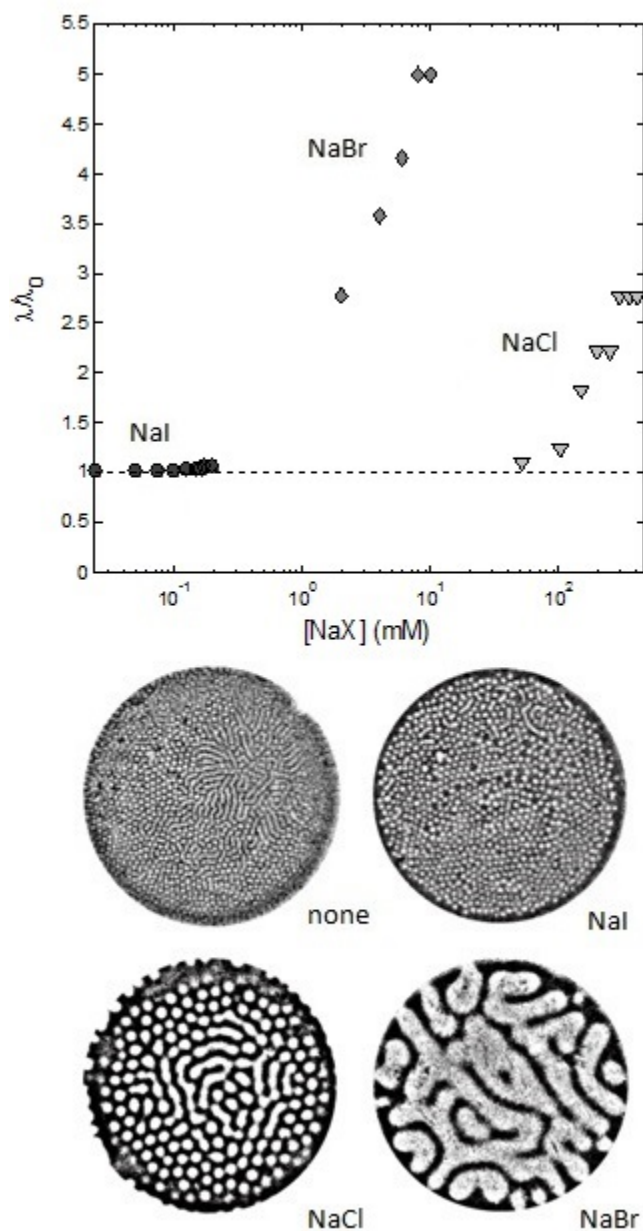
Figure 3.3: Wavelengths of Turing patterns in the CDIMA reaction-diffusion system are altered by additions of sodium halides. (a) Semi-log plot shows the ratio of wavelengths obtained at a given sodium halide feed concentration, λ, and at the original pattern wavelength, λ_0. (b)The Turing patterns corresponding to the largest wavelength patterns shown in the plot are displayed. To compare all on the same scale, these images have been processed with a local equalization filter. Reactor is 25 mm in diameter.

chloride reactions with the $-cv$ term. This term is used to simplify the detailed kinetics of the bromide-related [51, 52, 53, 54, 54] and chloride-related [55, 56, 57, 58, 59] mechanisms into a reaction rate law that is first order in v and first order in halide concentration. Since in our study we use a large excess of bromide and chloride compared to chlorite, we further simplify the expression to a pseudo-first order form. The parameter c then reflects the nondimensionalized rate constant of the reaction and the concentration of halide added. When c=0 this model reduces to the the commonly used two-variable Lengyel-Epstein (LE) model [60].

The introduction of bromide and chloride into the system leads to the formation of the series of interhalogen compounds $I_3^- \leftrightharpoons I_2X^- \leftrightarrow IX_2^- \leftrightharpoons X_3^-$ with the intermediates I_2, IX, X_2, where X is a bromine or chlorine atom [61, 62, 63]. The dihalogen species I_2 and Br_2 have been observed to affect the diffusion of their halide ions through the formation of the trihalide complexes. The triiodide complex slows the diffusion of iodide [64], and formation of the tribromide complex affects pattern stability in the Belousov-Zhabotinsky-Aerosol OT pattern-forming system [65]. The equilibrium constants for the reaction of iodide with the diatomic interhalogens IBr and ICl are four and eight orders of magnitude greater than that of the reaction of iodide with I_2, respectively [63]; thus we propose IBr and ICl also affect the effective diffusion of iodide. We incorporate this effect into the model by changing the relative diffusion constant, d, increasing it as the effective diffusion constant of iodide decreases.

Neither chlorite consumption nor altered diffusion alone was sufficient to qualitatively reproduce the observed experimental patterns. A decrease in effective iodide diffusion caused the pattern morphology to change from spots and stripes to honeycomb patterns. Spot patterns could not be accessed after honeycomb ones simply by increasing d. Including only the loss of chlorite failed to change the spot and stripe widths significantly. With
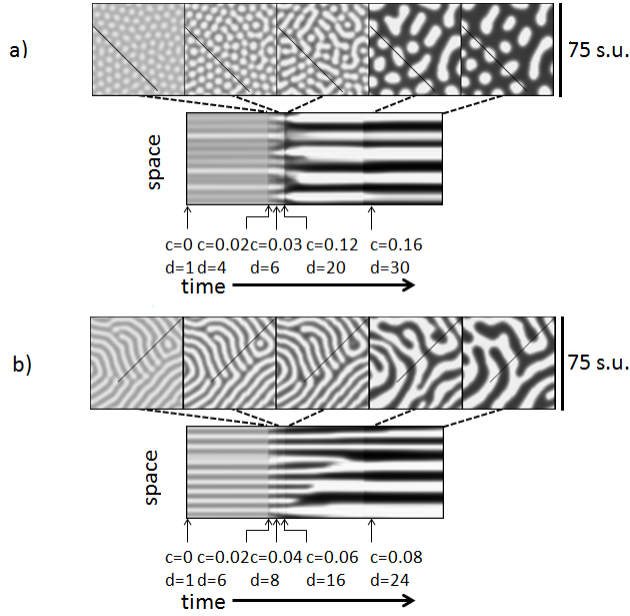
Figure 3.4: Simulations with Eqs. 3.1 and 3.2 with a simultaneous increase in c and d. Stable Turing patterns are formed in the model with parameters $d = 1, a = 12; s = 20; c = 0; b = 0.36$(a) and $b = 0.30$ (b). At the times indicated by the arrows, c and d are increased. Image sizes are 75x75 space units. a) Space-time plot for transitions from a spot pattern with a (c,d) of (0,1) to (0.02,4) to (0.03,6) to (0.12,20) to (0.16,30) shown with selected images immediately prior to transitions at t=5000, 5100, 5200, 6200 with the last image at 7200 time units. b) Space-time plot for transitions from a stripe pattern with a (c,d) of (0,1) to (0.02,6) to (0.04,8) to (0.06,16) to (0.08,24) shown with selected images immediately prior to transitions at t=5000,5100,5200,6200 with the last image at 7200 time units.

the inclusion of both effects, however, simulations were able to qualitatively reproduce an increase in pattern wavelength for stripes and spots (Fig. 3.4). Also, as observed in the experiments, we observed a loss of pattern above a certain threshold of the parameter c.

The main result that we present in this chapter is the experimental observation of large increases in Turing pattern wavelength. This is the first report in a chemical system where a pattern's intrinsic wavelength has been increased by more than a factor of two. The bromide addition results in a wavelength increase up to a factor of five. This development enables a new avenue for research on pattern to pattern transitions in CDIMA without relying on

spatial forcing. We are able to qualitatively reproduce these results by accounting for the effects that halide addition has on the kinetics of the reaction and the diffusion constants. Since CDIMA is the prototypical system for studying Turing pattern formation in reaction-diffusion systems, the potential impact of the study of pattern to pattern transitions in CDIMA is the development of insights for Turing pattern transitions in other systems. A deeper understanding of pattern to pattern transitions within the context of biomass patterns in arid ecosystems and those prone to fragmentation could lead to effective warning and management strategies for desertification and habitat fragmentation [42, 44].

Another area where changes in pattern wavelength would be of interest is the evolution of patterns on animal skin. It has been proposed that zebra stripes are an evolutionary advantage in the presence of biting flies, as the flies have preferences for certain wavelengths of stripes over others [46]. There is also evidence that natural selection determines the spot wavelength in guppies [45], and such wavelength selection may be a general phenomenon.

Chapter 4

Turing-Hopf Fronts

This chapter focuses on the invasion of bulk oscillations formed from the Hopf instability by a front of a pattern formed from two instabilities (Turing and Hopf). This is not the first example of non-uniform pattern domains or Turing-Hopf patterns. It is possible to have bulk oscillations or Turing patterns that do not uniformly fill the domain (e.g., partial synchronization seen in chimera states[66] or localized Turing pattern domains[67]) and also to have coexistence of Hopf and Turing domains in a system with both bifurcations. Turing and Hopf bifurcations occur together in a variety of systems. They can be found in models of biological (predator-prey dynamics[68], neural activation[69]) and physical (non-linear optics)[70] systems, and, of course, chemical systems, which include the prototypical CIMA system for Turing pattern formation[12] and the BZ-AOT system of our present study [34] as well as biochemical reaction networks [71] and electrodeposition[72]. When the Turing and Hopf instabilities interact, they can form patterns that are periodic both in time and in space. Some examples of mixed mode Turing-Hopf (MM T-H) interactions are oscillatory Turing patterns[50, 73], and oscillatory localized patterns [74], which have been obtained in experiments on chemical reaction-diffusion systems.

Experiments on such systems supported by theoretical work have established that when one localized domain is embedded or otherwise in contact within the other, the domain interface formed by the Turing pattern can be stationary [75, 76, 77] or it can move [77, 74], leading to the growth of one pattern domain at the expense of the other. Theory predicts that these domain interfaces can reverse spontaneously at a critical parameter value [78, 79] and that noise can increase the range within which destabilization can occur[80]. Recent experimental results have shown a phase-diffusion-like front between bulk oscillation and emerging Turing patterns[81]. MM T-H front structures between the domains have also been predicted [78].

Here we describe emerging Turing pattern domains that invade a region of bulk oscillation. Our major observation is the theoretically predicted MM T-H front structure, which we demonstrate by analyzing the amplitude (magnitude of brightness) of the pattern. In addition to the front structure, we observe different domain interface interactions, i.e., "frozen wave" dynamics [74] and a new phenomenon that we dub "reflecting waves".

4.1 Quasi-two-dimensional Turing-Hopf rings

Figure 4.1 shows the invasion of Turing patterns into a bulk oscillation domain via Turing-Hopf front rings in our quasi-two-dimensional reactor. The rings are the regions of bright amplitude (high concentration of oxidized catalyst) around the spots and spot-pairs. There is also Turing-Hopf advancement from the bubble in the upper right corner. Figure 4.2 details the development of the indicated target-shaped invasion structure. Turing patterns are present within the rings, while the bulk oscillation region is outside. A supplemental online video (available at *https* : *//github.com/deloragaskins/thesis_vids*) shows the time evolution of these patterns.

Figure 4.2 shows in more detail the development of one of the spontaneously formed invasion centers in Figure 4.1. Panel (A) shows the development of the pattern in space, with a uniform region in (a) giving way to a symmetry-breaking localized spot (b) and then surviving a bulk oscillation (c). Image (d) in this figure shows the Turing rings that form behind the Turing-Hopf ring front. The last image of this sequence shows the low-amplitude Turing patterns that remain after many minutes in this batch system.

Panel (B) of Figure 4.2 shows the behavior in time along a line through the localized spot in panel (A) and the surrounding region. Instead of the typical two-dimensional space-time plot with space and time axes, this is a three-dimensional rendering with the vertical axis representing the amplitude of the pattern, which is quantified using each pixel's grey scale intensity. A parula color map in yellow, green and blue is used to help with visualization of the amplitude intensity. The light regions in the images in panel (A) have higher pixel intensities and are more yellow in the false color of panel (B). Initially, the system is in a low amplitude uniform state. Then there is the onset of bulk oscillations with a relaxational waveform seen along the right-hand edge of the space-time plot parallel to the time axis. The localized spot forms in the wake of the first bulk oscillation, failing to relax to the reduced minimum like the rest of the bulk. This spot maintains a relatively constant amplitude while growing in space. When the bulk reaches its second oxidation spike, it interacts with the localized spot, leaving a dark center in the spot surrounded by light rings. The innermost ring adjusts over time until the width of the dark center is the same as the wavelength of the rest of the ring Turing pattern. The outermost ring has an amplitude that is larger than the inner Turing pattern rings, but lower than the bulk oscillation. The amplitude of the front ring oscillates, which is most visible along the front edge furthest from the labeled time axis.
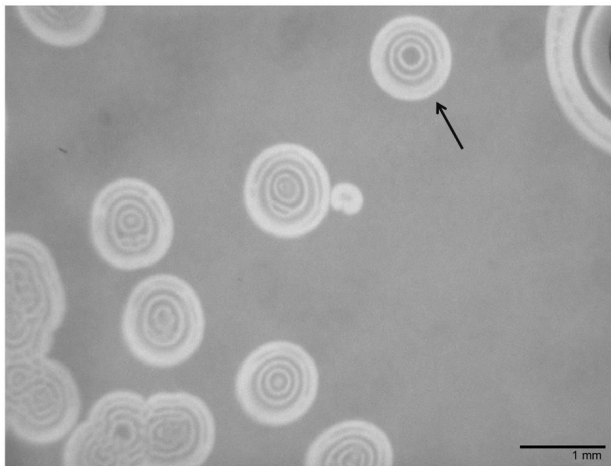
Figure 4.1: Invasion of Turing patterns into the bulk oscillation region. The arrow indicates which Turing-Hopf ring is being followed in Fig. 4.2. The time elapsed is 526 s.

4.1.1 Three-dimensional Turing-Hopf Balls and Shells

Figure 4.3 shows Turing pattern invasion via Turing-Hopf front advancement in a three-dimensional reactor (capillary tube). These images encode the transmittance of light that passes through the capillary tube, rendering a projection of any three-dimensional structures within. A bright, not exactly spherical ball with a dark center is shown in image (a), and this grows to touch the wall of the capillary (b). Turing structures form on the wall as the front continues to advance along the vertical axis of the capillary tube as shown in (c) and (d). The bulk reaches the bright peak of its oscillation in (e) and (f), which retards the front growth briefly as the Turing patterns become more distinct just behind the front ((g) and (h)). The front (shell) continues to advance and covers the reaction area, leaving Turing patterns in its wake. These patterns break up from stripes into spots over time, as seen in the final image in the figure.

Figure 4.4 also shows three-dimensional Turing pattern invasion via Turing-Hopf front advancement. As in Figure 4.3, these images show the transmittance of light that passes
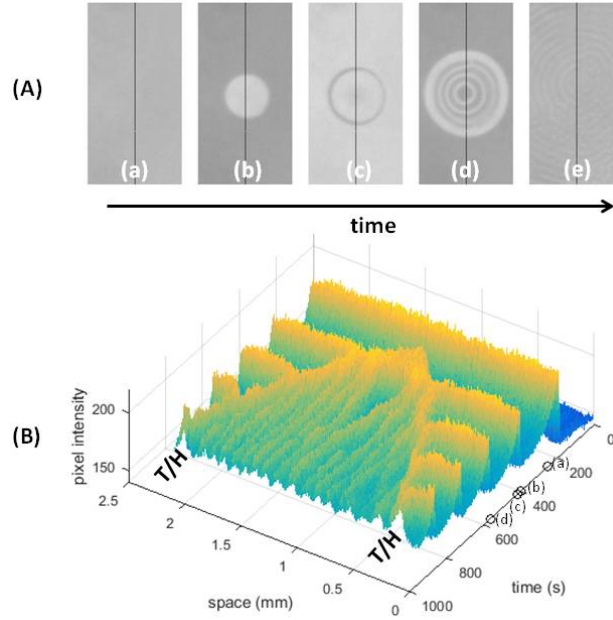
Figure 4.2: Quasi-two dimensional Turing-Hopf front growth. (A) Bulk oscillations (a) are invaded by a localized spot (b) that survives an interaction with the next oscillation peak (c) to develop into Turing patterns behind the Turing-Hopf front (d). This pattern growth is one of the many shown in Figure 4.1, the one the arrow points to. The final image shows the low amplitude Turing patterns that remain after the front has invaded at (e)1500 s. Images are 2.2 x 1.2 mm. The times corresponding to these images [(a)250 s (b) 397 s (c) 417 s (d)562 s] are marked in (B). (B) The amplitude of the line through the patterns in part (A) is plotted as a function of space and time (2.2 mm x 937 s).

through the capillary tube, which allows one to see a projection of the three-dimensional structures within. Image (a) shows half of a ball pinned to the wall of the capillary, a phenomenon seen more clearly in the isosurface from the reconstruction at this time in Figure 4.5(a). The ball continues to grow and hollow out (b). The bulk reaches its bright peak of oscillation, which interferes with the edge of the ball ((c) and (d)). The front (shell) continues to advance ((e) and (f)) as the Turing patterns behind the front become more distinct. The reconstruction for the pattern in (f) is shown in Figure 4.5(b). The last image in the sequence shows the Turing patterns that remain after the front advancement. The
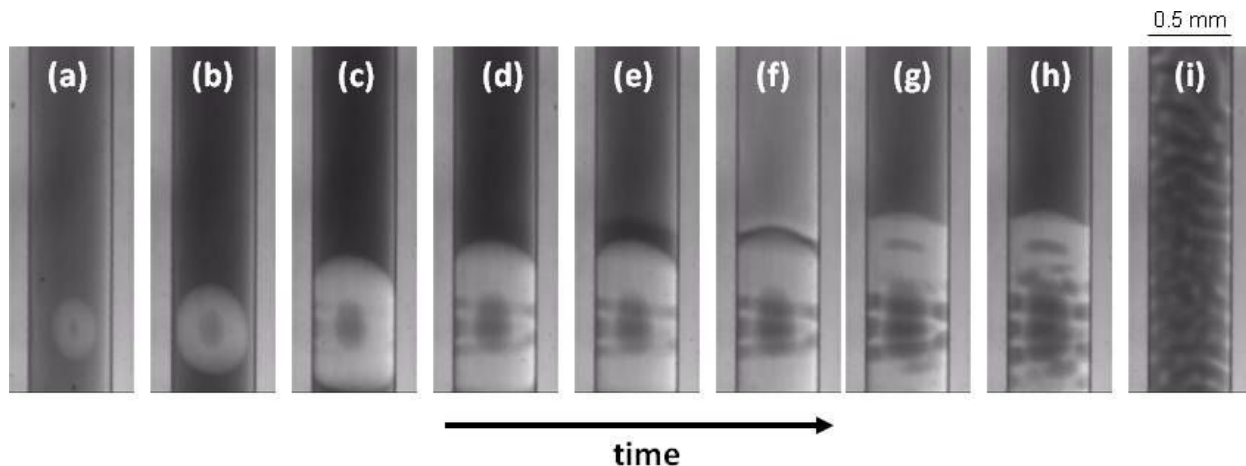
Figure 4.3: A Turing-Hopf ball grows into a bulk oscillation domain. Images are 2D projections of the ball in the capillary at the following times: (a)56 s (b)165 s (c)271 s (d) 316 s (e)331 s (f)351 s (g)387 s (h)425 s (i)1509 s. Turing patterns that remain after the growth of the front are shown at 1509 s.

nearly parallel fronts near the bottom of the reactor result from a change from Turing-Hopf front advancement to Turing pattern domain growth via frozen waves.

4.2 Discussion

4.2.1 Advancing Turing Pattern Domains

Turing pattern domains may invade bulk oscillation domains by several predicted and observed dynamical mechanisms. The most well-studied is the "frozen wave" mechanism, in which a phase wave slows to a stop as it approaches the established Turing pattern domain. When it stops, it becomes the outermost pattern stripe of the Turing domain. Frozen waves have been demonstrated in recent theoretical work by Berenstein and Carballido-Landeira, [79] where they focused on developing an understanding of how abutting subdomains of Turing and bulk oscillations interact in a reactive microemulsion. Frozen waves have been
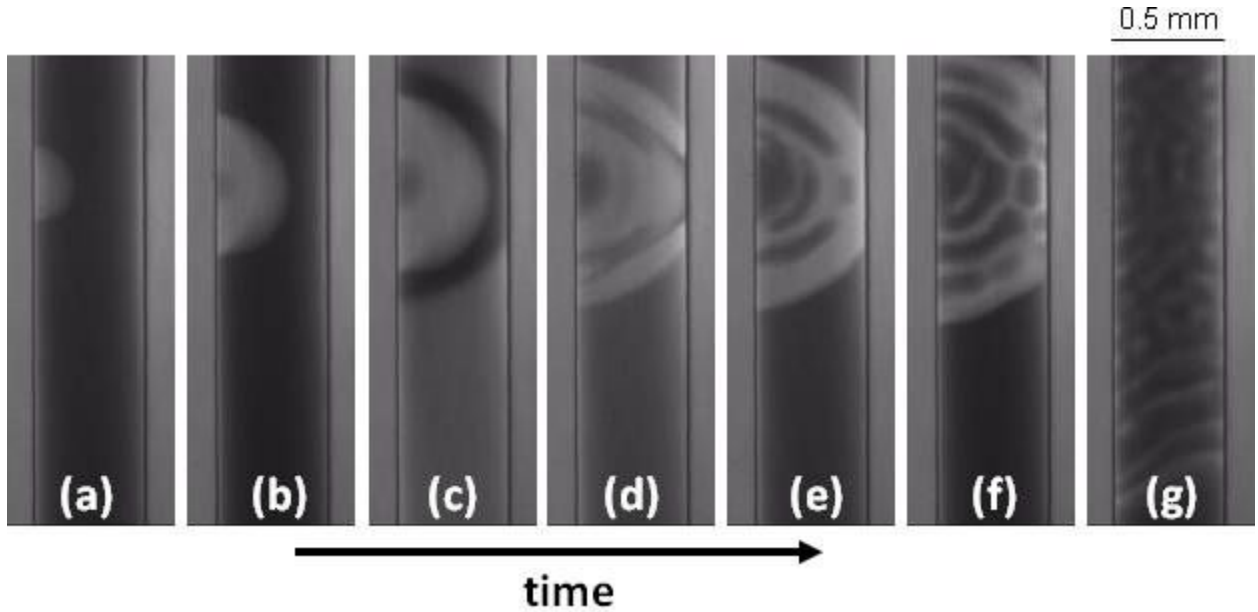
Figure 4.4: Invasion by pinned Turing-Hopf half-ball. Images are the 2D projections of the half-ball in the capillary at the following times: (a)118 s (b) 238 s (c) 285 s (d) 329 s (e)369 s (f) 502 s (g)1569 s. Turing patterns that remain after the growth of the front are shown at 1569 s.

reported in the BZ-AOT reactive microemulsion system with ferroin in octane and also in hexane [74].

A second mechanism of Turing advancement into bulk oscillation domains has the Turing pattern generating a phase wave. Turing spots in a quasi-one-dimensional system with the chlorite-iodide-malonic acid system have been observed to display this behavior[75]. Vanag also found a regime in the ruthenium-catalyzed BZ system where the outermost Turing pattern features generate phase waves behind which new fragments of Turing patterns emerge [74]. Turing-Hopf fronts generated in the FitzHugh-Nagumo model have also been predicted to generate phase waves as they advance [78].

Our work (Fig. 4.2) clearly shows a Turing domain and a bulk oscillation domain separated by a front structure. It is evident from these two features that the system is in a region
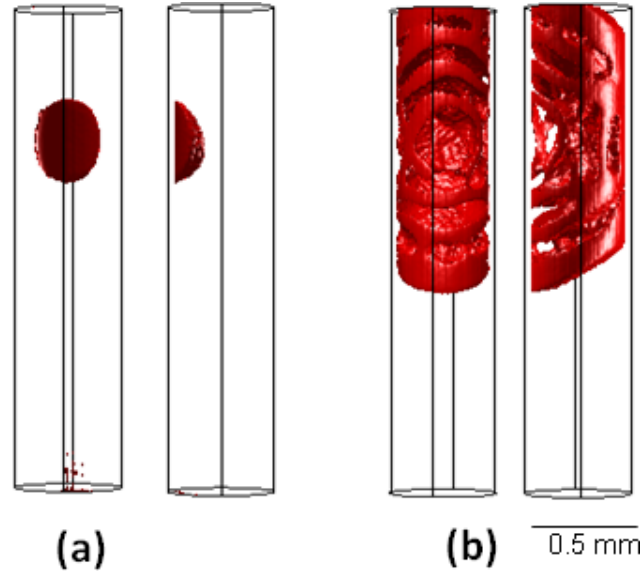
Figure 4.5: Three dimensional reconstruction of the Turing-Hopf half ball with (a) and (b) corresponding to the projections (a) and (f) in Fig. 4.4. The reconstructions are shown with their 90 degree rotations for clarity.

of parameter space where both a Turing instability and a Hopf bifurcation occur. However, the nature of the structure only becomes apparent on examining the amplitude of the front structure. The front structure oscillates, but with an amplitude between those of the Turing amplitude behind the front and the oscillations in the bulk. This is evidence that the Turing and Hopf modes mix and that the front is a Turing-Hopf structure.

In our batch system, we observe a change from Turing-Hopf advancement to frozen wave advancement. The rings at the bottom of Figure 4.4 show the planes added with each oscillation cycle. The supplemental video (available at $https://github.com/deloragaskins/thesis\_vids$) shows three different advancement mechanisms, which occur at different times. The first is the Turing-Hopf front, and the last is frozen waves. During the transition between these two features, the advancing front meets the advancing phase wave and retreats, a behavior we dub a 'reflecting wave'. This transition is due to the aging of the system, as there is no

replenishment of reagents.

4.2.2   Birth of the Spatial Structures

In this region of parameter space, shown by a typical example in Figure 4.2, a uniform, non-oscillatory state is first observed, which then becomes unstable, leading to relaxation oscillations in the bulk.

The bulk oscillation becomes unstable to localized structures, which do not have a characteristic wavelength and show no discernible oscillations. The internal structure may collapse, creating a hole before or after the oxidation spike of the following bulk oscillation. The first Turing ring or internal ball forms around this region, and the patterns continue to grow in the form of rings left behind the advancing front. This can be more clearly seen in the supplemental video (available at *https* : *//github.com/deloragaskins/thesis_vids*).

Typically, Turing patterns arise from perturbations to the uniform steady state. However, the Turing patterns that form here do not do so from the uniform steady state. We interpret the destabilization of the bulk oscillations to give spatially localized structures to be a result of the Turing instability interacting with the Hopf bifurcation. Similar growth structures have been observed when localized Turing structures form and are embedded in a non-oscillatory domain in the subcritical Turing regime of the chlorite-iodide-malonic acid reaction [67].

4.2.3   Geometric Considerations

In Figure 4.1 a gas bubble can be seen in the upper right corner. In the supplemental video (available at *https* : *//github.com/deloragaskins/thesis_vids*), we can see that along with the spot structures a light front begins to form at the interface of the bubble and the edge of the solution, an example of an edge effect. This front behaves as the spots do, expanding

away from the interface. The phase wave slows down as it approaches the edge, and patterns are generated behind that front. The two fronts meet and are replaced by a Turing stripe. Later, the outer front continues advancing away from the bubble.

Edge effects are also possible in three dimensions, as shown by the pinning of the half-ball. We note that both the ball and the half-ball (Figure 4.4) when they meet the boundary are traveling on a curved surface. Turing patterns on curved surfaces have attracted significant recent interest.[82] Perhaps the most striking feature about these Turing-Hopf fronts is the regularity of the Turing patterns that they lay down. These appear to the eye as circles (Figures 4.1 and 4.2), because of the circular nature of the initial spots in two dimension. In three dimensions they are not perfect spheres or hemispheres, but are close to these shapes. Or-Guil and Bode note that the honeycomb patterns generated by Turing-Hopf fronts in the FitzHugh-Nagumo model are much more regular than the honeycomb planforms of the Turing patterns that appear from the steady state [78].

4.3 Conclusions

We have demonstrated by considering the amplitudes of the pattern components that Turing domains can advance into a bulk oscillation region following a Turing-Hopf front. We have shown this in two dimensions and explored what the three-dimensional analogs look like, both for a ball that forms in the center of the cylindrical capillary and ball that is pinned on on the wall, both of which ultimately develop advancing Turing-Hopf front shells.

Pinning to the wall and other edge effects suggest a potential for planform control by strategic placement of barriers. Planform control could be useful for systems that have Turing and Hopf bifurcations like electrodeposition at surfaces[72] .

Chapter 5

Standing Waves

5.1   Introduction

In this chapter, we present another type of pattern invasion (modulated standing waves) .
Like in the previous chapter, a bulk oscillating domain is being invaded by a pattern with a
spatial lattice. They are not Turing patterns, though, but appear to be standing waves that
are not perfectly in sync over the whole space. Multiple types of waves have been observed
in this system, including standing waves[83], [84]. Localized domains of standing waves have
also been reported[85]. Standing waves whose nodes are slightly out of synchronization with
their neighbors are known as modulated standing waves and have been predicted to form as
a result of interaction [86] between Hopf and wave instabilities [87].

In this chapter, along with the experimental results on the birth (invasion into a spa-
tially homogeneously oscillating region) of standing waves, we present their death (transi-
tion to spirals) in a closed system. We show an invasion pathway for localized structures to
form standing waves that overtake the Hopf domain. The standing waves occur in a region
bounded by a traveling wave envelope which separates the invading standing waves from the

Hopf domain. We also examine the transition of the standing waves to spiral structures and connect this to a generic chemical model.

5.2 Results and discussion

5.2.1 Birth of standing waves

Localized spot structures form in a bulk oscillation region and evolve to form expanding circular domains of standing wave and modulated standing wave structures in Fig. 5.1. The oscillations are relaxational in nature. The first spike of oxidation occurs just before formation of the expanding circular front, which is shown in (A). The inter-spike intervals decrease as the reaction proceeds. The front separating the spatial structures from the homogeneous region speeds up as the bulk relaxes. Standing wave formation occurs behind the expanding front (B). A lattice structure then forms, as seen in (C).

Modulated standing waves (MSW) are observed to develop from the standing waves as a difference of phase develops within the domain. The nodes of the lattice of standing waves are oscillating and annihilate with the waves of the neighboring nodes. The modulation separates the domain into zones of (i) white spots with dark background or (ii) white background with some dark spots. The desynchronization appears to travel in the direction opposite to the expanding traveling wave. A series of zones of type (ii) appear to be moving inward, as seen in the supplemental video for this figure (available at *https* : *//github.com/deloragaskins/thesis_vids*).

The oxidized zone, which is marked with arrows, is forming in (C) and becomes clearer in (D). This is seen in the space-time plot of the standing waves, which are initially oriented vertically (i.e., in-phase). Then, near the mark for (B), they lose synchrony with their
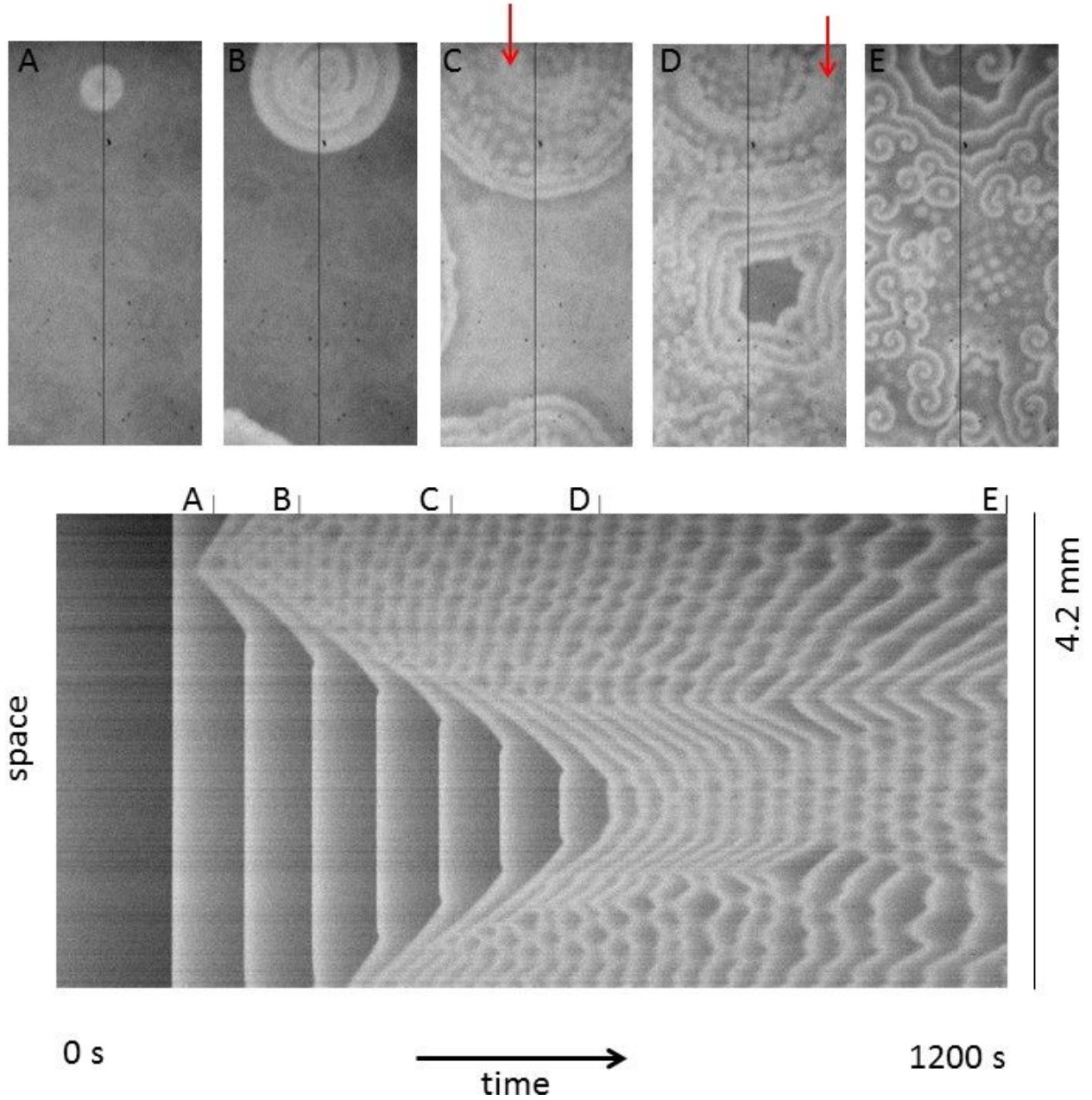
Figure 5.1: Invasion of modulated standing waves into into the bulk oscillation region. Images A-E show the invasion of the spatial patterns from the edges into the bulk oscillation region in the center. These images correspond to the times marked in the space-time plot below. The space line in the space-time plot is the vertical dark line in the series of images. Total time elapsed is 1200 s. Images are 2 mm x 4.2 mm. The parameters ω and ϕ_d are 12.35 and 0.45 respectively. The greyscale reflects the ratio of ferriin to ferroin, with the light regions corresponding to a high [ferriin] and dark ones to high [ferroin].

47
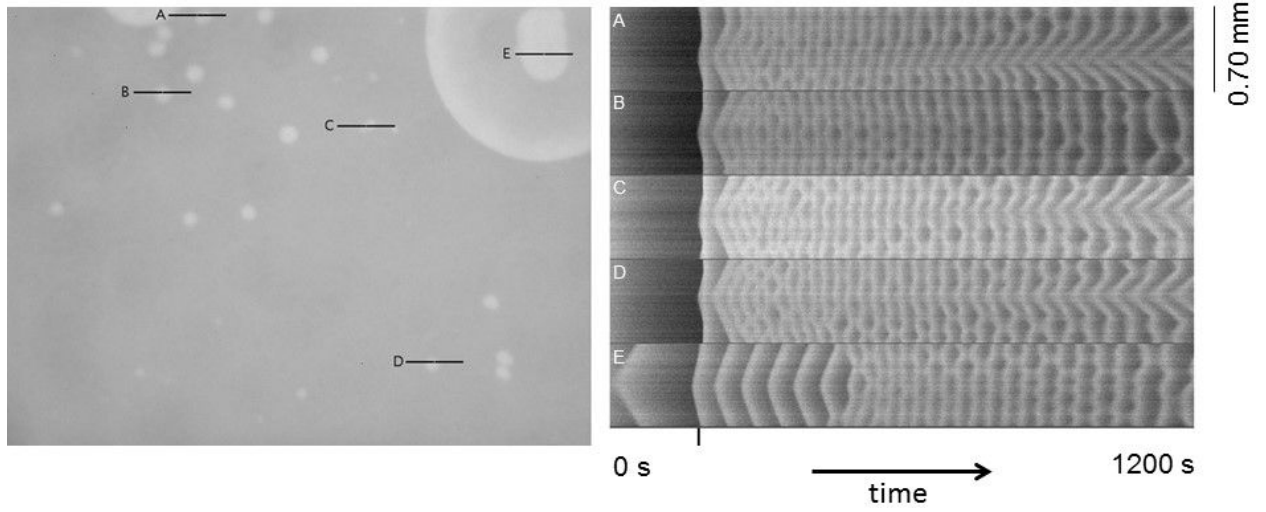
Figure 5.2: Invasion of modulated standing waves into the bulk oscillation region. The left image shows local spatial structures formed prior to the formation of the modulated standing waves. Image size is 7.11 mm x 5.33 mm. This image was captured at the time marked in the space time plots on the right (184 s). The space-time plots on the right illustrate the evolution in time of the behavior on the individual lines A-E in the image on the left. Space time plots are each 0.70 mm x 1200 s. The parameters ω and ϕ_d are 11.11 and 0.46, respectively.

neighbors, creating the zones described above, which results in an apparent direction of propagation indicated by the development of a slope in the modulated waves. Also shown in image (D) is the formation of traveling waves near the center of the image between the standing wave structures. Spiral structures form in the domains of the standing wave structures. The space-time plot shows that the traveling waves that form at the boundary of a standing wave domain interfere to form standing wave structures. These standing waves and spirals are shown in (E).

A notable, and typical feature of the invasion of the standing wave structures can be observed in Fig. 5.2. The spatially localized spots that ultimately form standing waves appear at the same time, just prior to the peak of the relaxation oscillation. The upper four space-time plots in Fig. 5.2 illustrate this behavior. Not all of the expanding structures form standing waves from the beginning; for example, a target pattern is shown in the lowermost space-time plot (E).

The invasions presented in Figs. 5.1 and 5.2 do not involve the oxidized uniform state. Instead, there are circular waves of oxidation that propagate into the bulk. The standing waves develop behind that front. We suggest that these waves are phase diffusion waves, as the leading front is observed to speed up as the relaxation oscillation in the bulk progresses, rather than propagating at a constant speed. Likewise, the interference of the traveling waves in Fig. 5.1 is not typical for trigger waves, in which the leading fronts annihilate, as they cannot propagate into each other's refractory region. Both of these invasion types differ from the localized standing waves that invade the bulk oscillations of the BZ-AOT [74] and CO oxidation [88] systems, which do not have a defined wave envelope as a front between the bulk oscillation and standing waves. Figure 5.2 shows that multiple localized wave domains occur at the same time. We interpret this behavior as resulting from the spatially distributed noise that is always present in the experimental system acting as a perturbation that can

grow within certain excitable windows in the phase of the bulk oscillation.

5.2.2 Death of Modulated Standing Waves
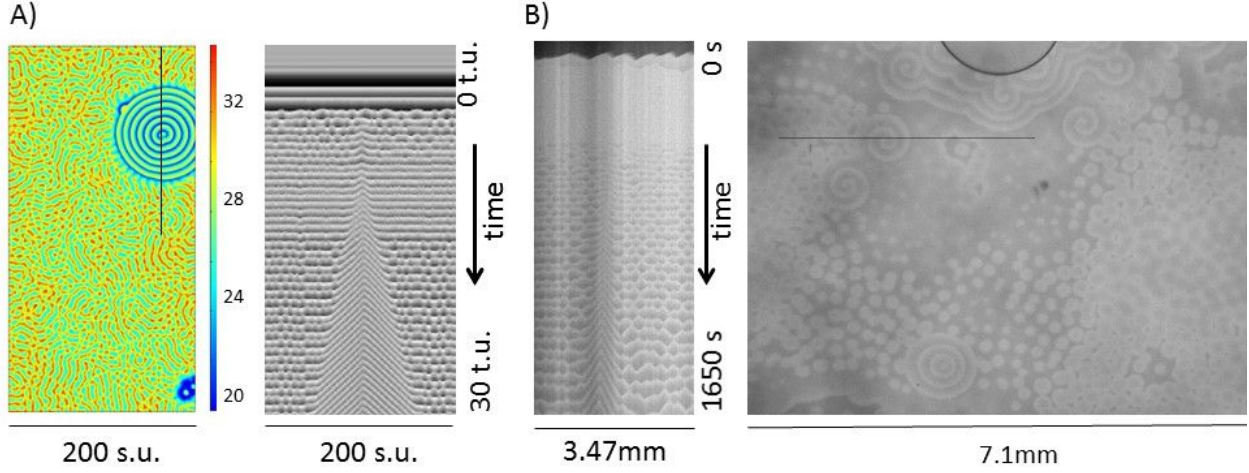
Figure 5.3: Death of standing waves. A) False color image on the left shows a numerical simulation of standing waves being overtaken by spirals in the Peña-Bestehorn model. The values of the variable U are indicated with the color bar. Numerical parameters are $A = 3, B = 5.6, p = 1, D_U = 5, D_V = 0.05, D_W = 1$. The initial conditions are set to the steady state for variables V and W, while U is perturbed from the steady state (Uss) to be U(x,y) $= Uss + (1 + 0.1*\text{rnd}(x, y))$ where $\text{rnd}(x, y)$ is the random distribution with mean=0 and range=1. Space-time plot shows the evolution in time of the line of the image on the left. Image size is 200 x 400 space units. B) Experimental observations of standing waves overtaken by spirals are shown on the right. Experimental conditions are:[MA]=0.25, [H$_2$SO$_4$]=0.38, [NaBrO$_3$]=0.2M, [Ferroin]=0.01M. The parameters ω and ϕ_d are 10.07 and 0.44 respectively. Image size is 5.3 x 7.1 mm. Space-time plot on the left shows the evolution in time of the line in the image on the right.

In our experiments, the BZ-AOT experimental medium is a far-from-equilibrium dynamical system within a batch reactor, and so over time the system must approach and ultimately reach equilibrium. Previous experiments in the BZ-AOT system have shown that standing waves can transition to traveling waves [83, 84]. The wavelength of the pattern was halved in the transition observed by Kaminaga *et al.*, and transitions to spirals and packet waves were

reported by Bánsági *et al.* While there have been numerical investigations of standing waves [84, 83, 74] and modulated standing wave behavior [86, 89] in chemical reaction-diffusion systems, the transitions studied have not, to our knowledge, included spiral formation. Peña and Bestehorn [86] used the following three-variable model to observe the interaction between Hopf and wave instabilities, generating modulated standing waves and different types of spirals, depending on the proximity to the codimension-2 point of the instabilities. The variables U, V, and W represent chemical species with diffusion coefficients D_U, D_V, D_W respectively. A and B are input reactants of the model, and p is a ratio of kinetic rate constants.

$$\frac{\partial U}{\partial t} = -2U + 3BW + D_U \nabla^2 U \tag{5.1}$$

$$\frac{\partial V}{\partial t} = U - VW^2 + D_V \nabla^2 V \tag{5.2}$$

$$\frac{\partial W}{\partial t} = A - (3B + p)W + 2VW^2 + D_W \nabla^2 W \tag{5.3}$$

We have used their model to qualitatively reproduce the transition we observe experimentally in our chemical system of modulated standing waves to spiral structures. We achieve this by perturbing the system far enough from the U variable steady state with random spatial noise. The space-time plot in Fig. 5.3A shows initial bulk oscillations and the formation of modulated standing waves. As time progresses, a single spiral forms, which then proceeds to overtake the rest of the domain. An experiment is shown on the right for comparison. In the experiment, the spiral formation arises well before the desynchronization of the standing waves and their transition to traveling waves. This observation is in contrast to the transition behavior modeled and observed by Kaminaga *et al.*[83], where the whole domain transitioned to traveling waves simultaneously.

5.3 Conclusions

In this chapter, we have shown the invasion of the bulk medium by modulated standing waves, which are in turn overtaken by spirals. Invasion of standing waves has been reported previously in the BZ-AOT system [74] and in CO oxidation [88]. The invasion route here differs in the manner by which the standing waves invade, in this case behind a traveling wave front. We also report the observation of many nearly-simultaneously appearing localized structures prior to the spike of the relaxation oscillation. This phenomenon is consistent with the interpretation that at this point in the phase of oscillation, the oscillator is vulnerable to perturbation. Further work must be done to connect these results with Floquet analysis of a more chemically realistic model of this system.

In addition to invasion, we have qualitatively modeled the transition of standing waves to spiral traveling waves. This scenario differs from previous numerical and experimental work in that individual spiral structures form instead of the whole domain switching to traveling waves. The existing literature on standing wave defects is sparse, and we leave to future work the details of how individual defects form to allow spiral formation.

Turing patterns have been found experimentally in the present system [90, 27] at lower H_2SO_4 concentrations. The invasion of Turing patterns into bulk oscillations has gathered recent interest [91]. Our interpretation of this invasion of standing waves into the bulk oscillation relies on the wave and Hopf instabilities, although additional interaction of the Turing instability could be responsible for the development of the lattice structure that develops after the first standing waves. Turing-wave interactions result in modulated standing waves as well [92]. Theory predicts that advection could be used to discriminate which instabilities are present under our conditions, which could be explored in future work [93].

Chapter 6

Continuing Work on Patterns

This chapter focuses on patterns which have been observed but require more work towards a complete narrative. Segmenting spirals have been observed in the quasi-two dimensional system, and the first section focuses on the study of the three dimensional analog of these patterns. The second introduces new pattern interaction that generates growing rings and forms Turing patterns with the settling of waves. The growing rings are distinct patterns from the bubble waves reported by Vanag and Epstein [65].

6.1 Three dimensional segmenting scroll waves

Spiral waves and target patterns were the first spatiotemporal patterns observed in the BZ reaction. Spirals are an inherently two dimensional phenomenon where a wave rotates about the spiral tip. The extension of the spiral in a three dimensional space is a scroll wave or ring, depending on the geometry of the scroll filament. A spiral tip is a point (OD) and a scroll filament is a line (1D). The sketch from Ref. [4] in figure 6.1 (a) shows a scroll wave with the filament touching both the top and the bottom of the rectangular box. Each

horizontal planar cut has the shape of a spiral. Figure 6.1(b,c) shows a scroll wave in the BZ system from [5]. Figure 6.1(b) is acquired by letting light pass through the scroll wave, so it is a two dimensional projection of the scroll wave. Figure 6.1 (c) is a tomographic reconstruction of a set of such projections. Each planar cut is a spiral and the filament is depicted by a black line. The filaments of scroll waves can twist, bend, knot, and do a variety of interesting things topologically. A scroll ring is a scroll wave with a circular filament. This is represented in 6.1(d,e) as a schematic and also a two dimensional projection from the work of [6]. The wave envelopes generated at the filament of Fig. 6.1 are continuous planes.

Dash waves are an example of discontinuous wave fronts, and were first reported in the the BZ-AOT system in [94]. They can be generated by Turing patterns [95] or by the singularity at a spiral tip in segmented spirals [7] as seen in figure 6.2. The segments grow until they attain a characteristic length and then they divide into two. This can be seen in the stroboscopic image (c) of the spiral development in time of (a). The interaction of instabilities that leads to the formation of the dash waves has not been determined, though among competing models, one that relies on two subsystems, one excitable and one Turing, provides for more robust dash wave formation [96].

The standard preparation of the reverse microemulsion separates out the reactive components into two different solutions ($MA + H_2SO_4$ and BrO_3 + ferroin). For certain conditions, the solutions can be stored separately overnight and patterns will still form. This is not the case for the segmenting patterns, which have only been observed with freshly prepared solutions with bathoferroin as the catalyst. Some fraction of the droplets in the microemulsion form clusters of droplets during mixing. As the solution ages, these droplet clusters break apart. The additional steric bulk of the ligands on the bathoferroin is thought to maintain the droplet clusters and support the formation of the segmenting patterns, which only start to segment after some time has elapsed in the reaction. A polymer, polyethylene oxide, has

been added to the system and increased the lifetime of these patterns from the typical 2-3 hours to 10-12 hours. [20]

How these dash patterns might propagate in three dimensions is not yet known, and the preliminary experiments in this section show the formation of segmenting scroll rings and waves. The solution conditions for this section are [MA] = 0.3 M, [H$_2$SO$_4$] = 0.2 M, [NaBrO$_3$]= 0.18 M, [BF]=5 mM, $\omega = 13.890$, $\phi_d = 0.451$.

Figure 6.4 shows a two-dimensional projection of a scroll ring and how it changes as the innermost wave completes one period about the filament. The initial wave envelope is continuous, but by t=38min (750s after the first image in that sequence) the wave has started to break.

Figure 6.5 shows a pair of scroll rings; their cores are marked in (a) with arrows. The cores face front in the projections in the top row. The capillary is rotated by 180 degrees in the reconstruction beneath. At time (a) the wave envelopes are continuous. Initial holes in the inner wave envelope have started to form by (b) and a number more form by (c). Holes in the second wave are seen in (d). Additional breaking up occurs in (e) and (f).

A challenge that remains is obtaining control of the initial geometry of the scroll rings so that the topology of the scrolls can be seen more clearly as they break up. Currently the scrolls form spontaneously, allowing for multiple scroll formation in a narrow area. This makes it difficult to resolve the segmenting areas. This problem could potentially be remedied by touching the solution with a silver wire, or with light if the photosensitive catalyst ruthenium bipyridine is included in the recipe. These approaches could be used to initiate the formation of a scroll. Another potentially interesting thing to do would be to align the scroll with an electric field, which has been done in the BZ system [97]. The narrow diameter of the capillaries would mean that small electrodes such as microelectrodes would need to be used.
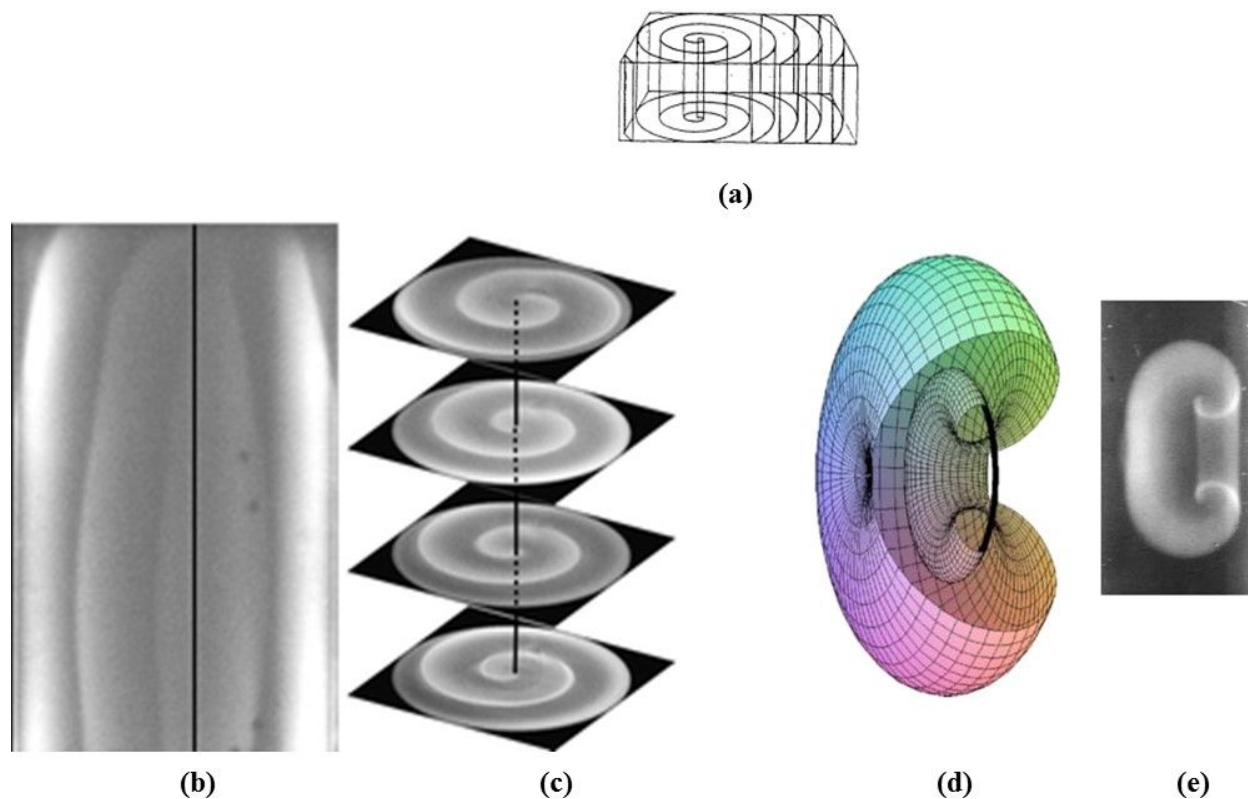
Figure 6.1: (a) Representation of a scroll wave [4] (b,c) Projection of scroll wave shown from the side orthogonal to the spirals in the BZ reaction (b) and reconstructed slices from that scroll wave (c). Black line represents the filament [5]. (d,e) Graphic representation of a scroll ring (d) and scroll ring (e). Black line represents the filament of the ring. [6]
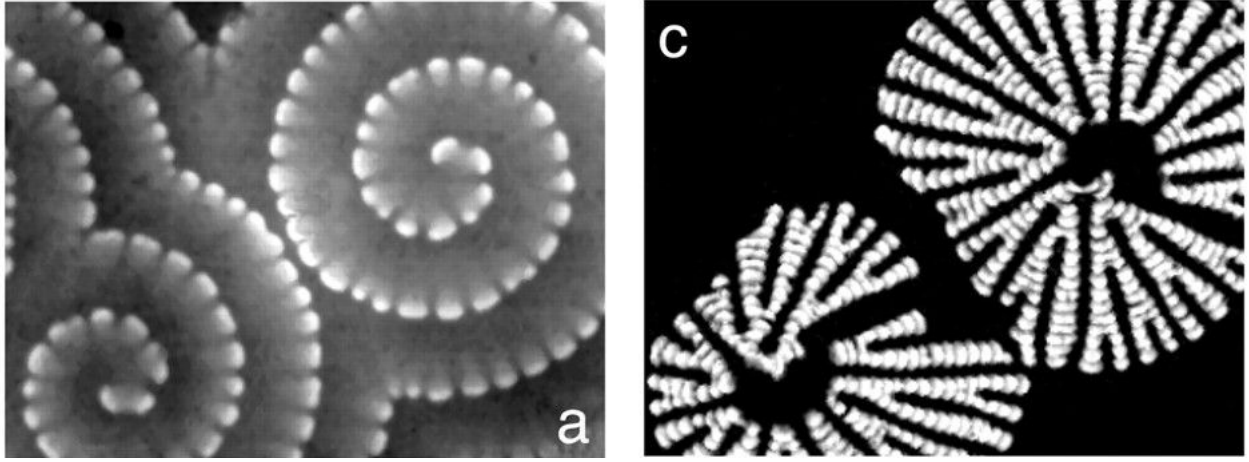
Figure 6.2: (a)Segmented spiral in a quasi-two dimensional BZ-AOT system (c) Stroboscopic images of the pattern in (a). [7]
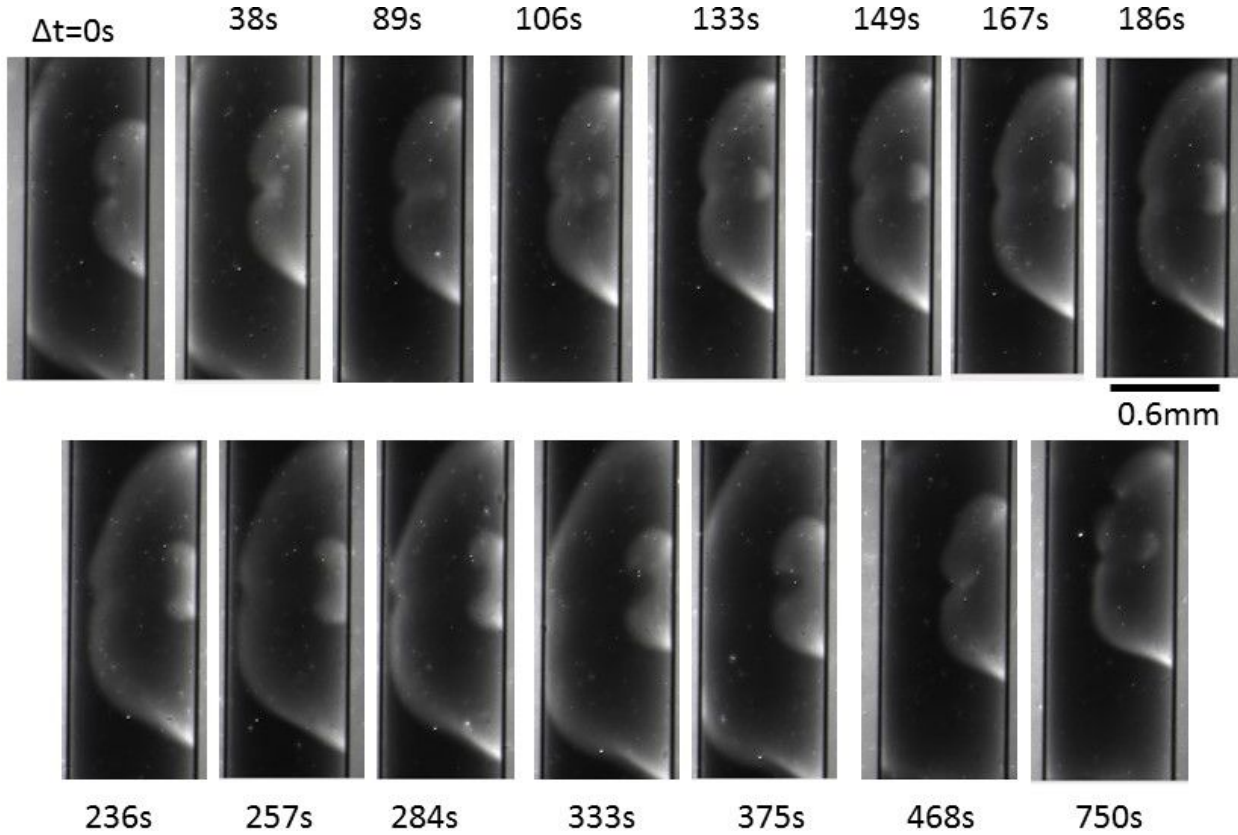
Figure 6.3: One period of a scroll ring in BZ-AOT from Δ t=0 to 468s, Segmentation occurs in image at Δ t=750s

.
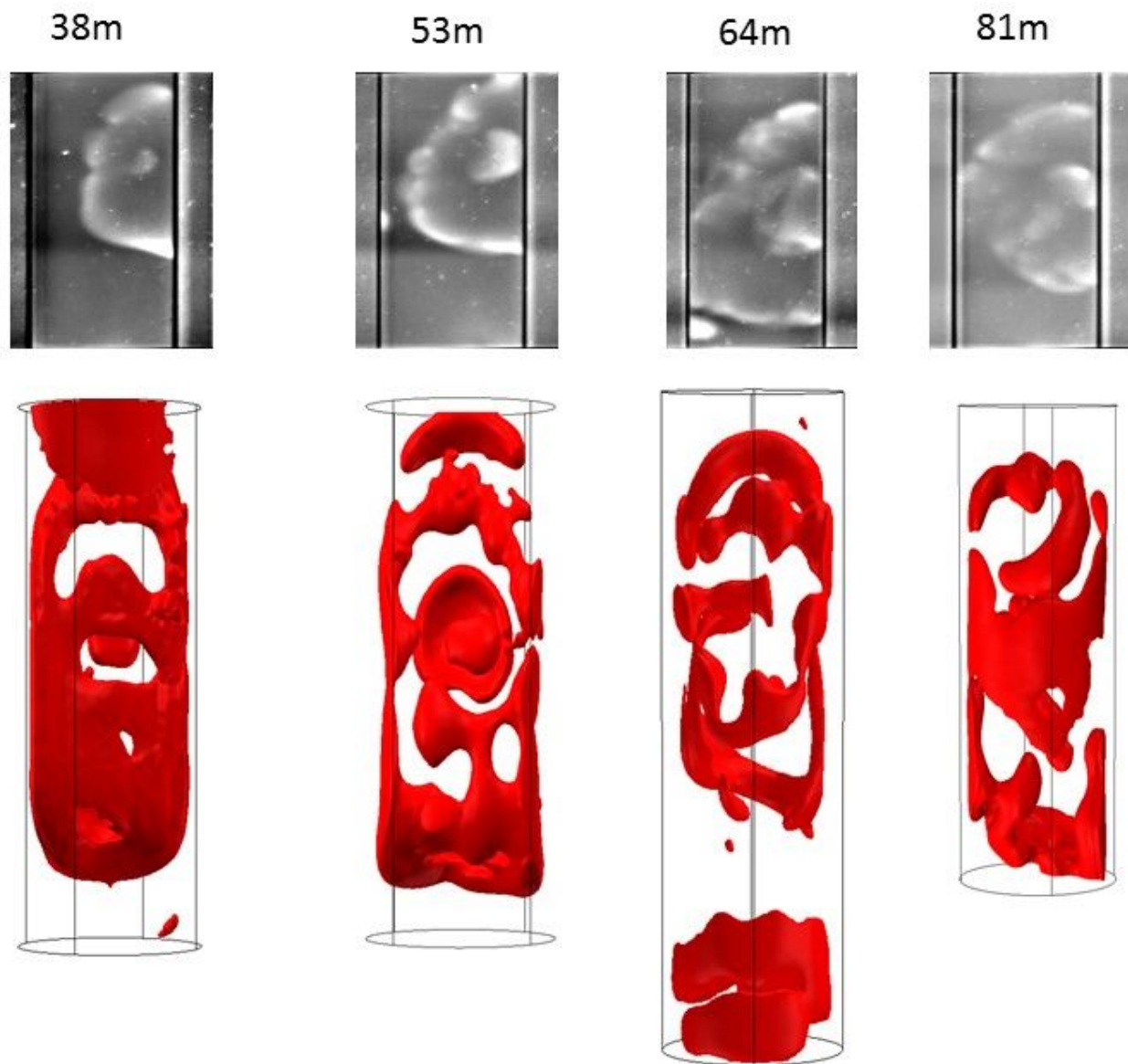
Figure 6.4: Progressing segmentation of scroll ring in Figure 6.3. Top row shows two dimensional projections of the segmenting ring. Bottom row shows the corresponding three dimensional reconstructions.
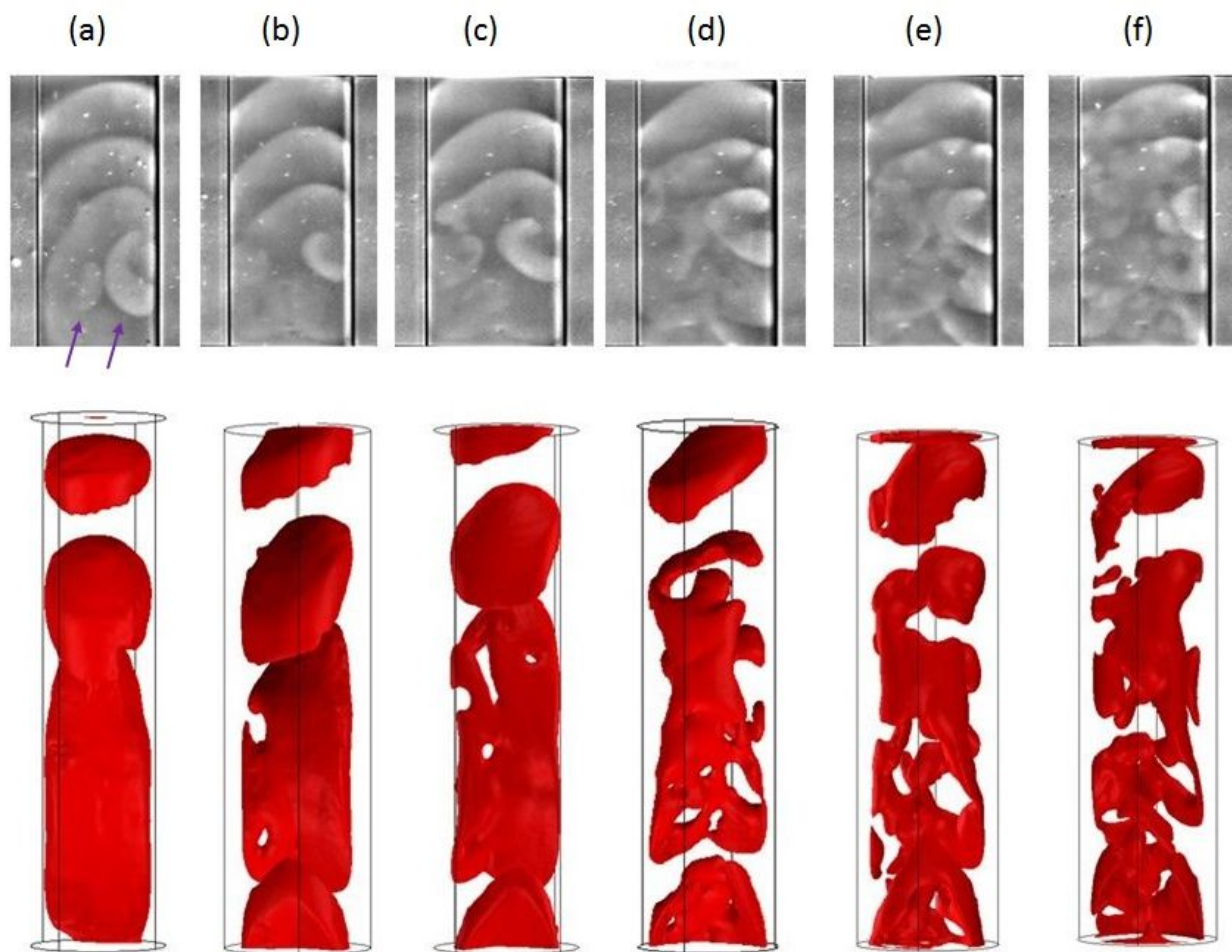
Figure 6.5: Progressing segmentation of a pair of distorted scroll rings. Each spiral core is indicated by an arrow in (a). Top row shows two dimensional projections of the segmenting ring. Bottom row shows the corresponding three dimensional reconstructions. Capillary diameter is 0.6 mm. Times are (a) 25s (b) 66s (c) 71s (d) 85s (e)90s (f) 94s.

6.2 Growing rings and settled Turing patterns

The development of the pattern in Figure 6.6 starts in a very similar way as the Turing-Hopf rings in chapter 4. When the first oxidation peak occurs in the reaction, it causes the previously uniformly colored spots to form rings. But then, instead of the inner ring developing into a Turing stripe, it becomes nearly stationary for a time while the outer ring propagates outward. Then for both rings, backfiring occurs at the time indicated by the arrow. The backfiring can be seen as both rings propagate inward and outward relative to the circle center. At this time there is the development of a white front pinned to the edge of the expanding circle. This is strikingly similar to the Turing-Hopf rings. When two of these fronts meet they form an interference pattern. There is then an interesting collapse of the wave as it settles into a striped Turing pattern. Over time these stripes break up and become spots.

Figure 6.7 shows another pattern, "growing rings". There is the development of a spot which becomes a ring that propagates outward. This front has a transverse instability which grows as it propagates. When the bulk oscillation approaches the pattern, it slows and develops into a traveling wave. Because of the meeting of the non-circular outwardly propagating wave and the inwardly propagating wave, spots remain after the fronts meet. This spot then grows into a ring itself at the same time as the original ring reappears. At t=1000 spots form because of the interaction with the bulk oscillation at t= 860. Eventually the spots stop growing into rings and become nearly stationary.

Figure 6.8 is another representation of the set of growing rings in the previous figure. This plot is a three dimensional space-time plot which shows two spatial dimensions and the z axis represents time. The green represents the light area in the previous figure. Initially, there is a cone that is growing until the first bulk oscillation. This nearly cylindrical shape

slowly increases in radius. The growing rings become evident after the first oscillation. After these rings start expanding, the interior ring reforms and also expands.

The patterns in figures 6.9 and 6.10 have characteristics similar to both settling Turing patterns and growing rings. Both have backfiring of the exterior ring towards the center.The interior of the pattern settles into Turing patterns, but not concentric circles. Also, they do not develop a bright front as in the first case of the settled patterns and like the Turing-Hopf fronts. Instead a growing ring front forms. In figure 6.10, this happens for the duration of several bulk oscillations.
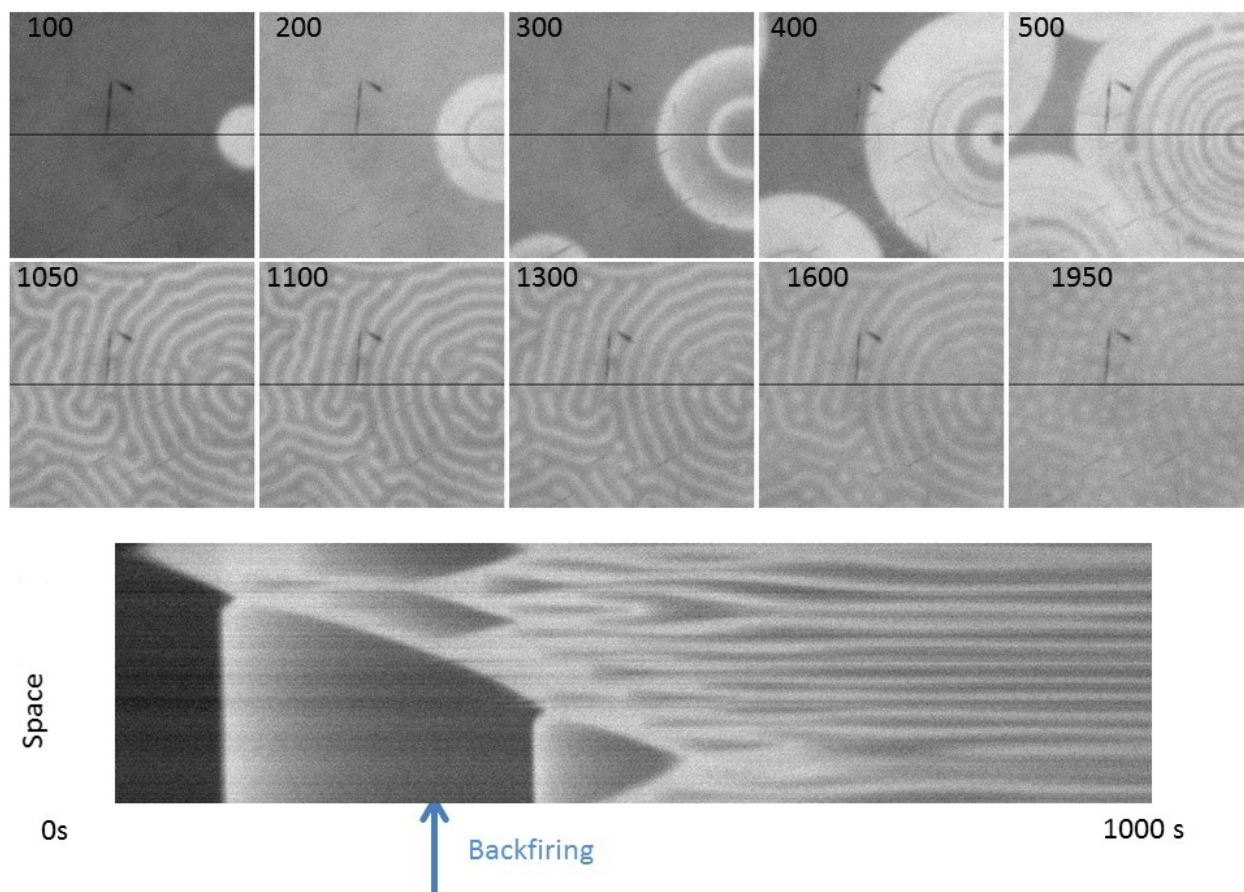
Figure 6.6: Settled Turing pattern. The upper sequence of images shows the development of the quasi-two dimensional spatial patterns. The lower space-time plot shows the development of the black line from the images over time. The arrow indicates the time when backfiring occurs. Solution conditions:[MA] = 0.25 M [H$_2$SO$_4$] = 0.2M [NaBrO$_3$]= 0.2 M [ferroin]=10mM $\omega = 12.34$, $\phi_d = 0.400$. Images are 1.7mm x 1.7mm.
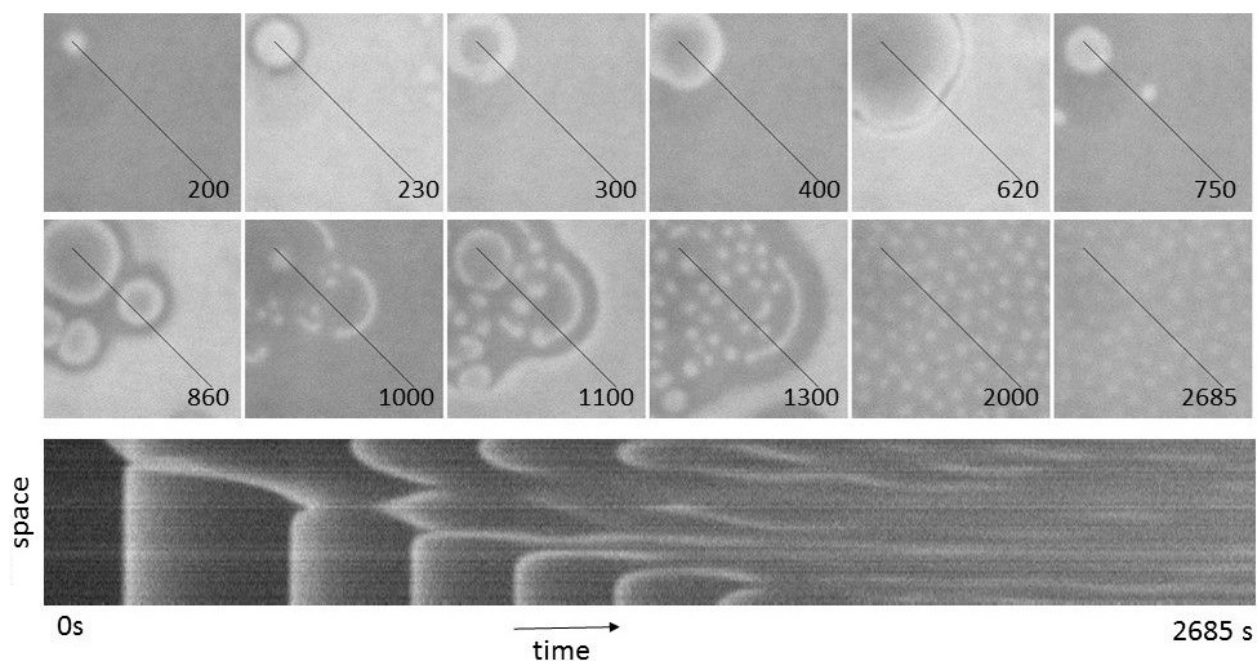
Figure 6.7: Growing rings in BZ-AOT. The upper sequence of images shows the development of the quasi-two dimensional spatial patterns. The lower space-time plot shows the development of the black line from the images over time. Solution conditions are [MA] = 0.25 M, [H$_2$SO$_4$] = 0.2M, [NaBrO3]= 0.2 M, [Bathoferroin]=10mM, $\omega = 12.34$, $\phi_d = 0.299$, Images are 1.7mm x 1.7mm.
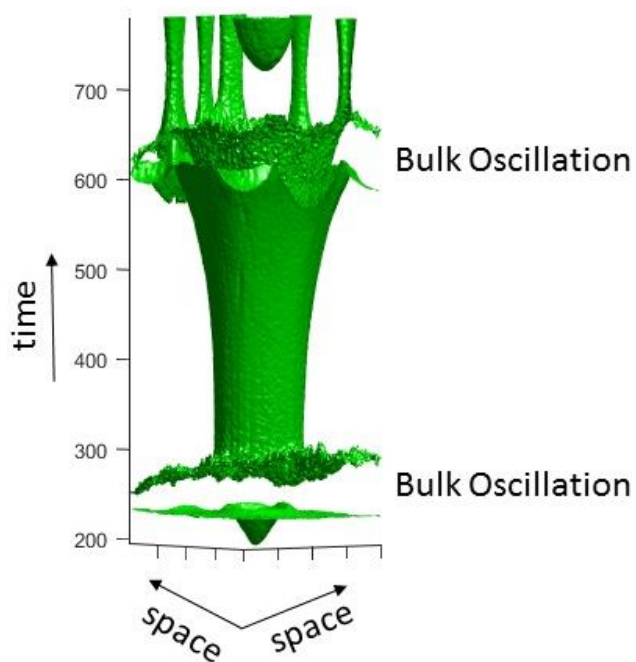
Figure 6.8: Three dimensional representation of the pattern in Figure 6.7. The z direction is time and the x and y axes are space. (1.4mm x 1.4mm x 761 s)
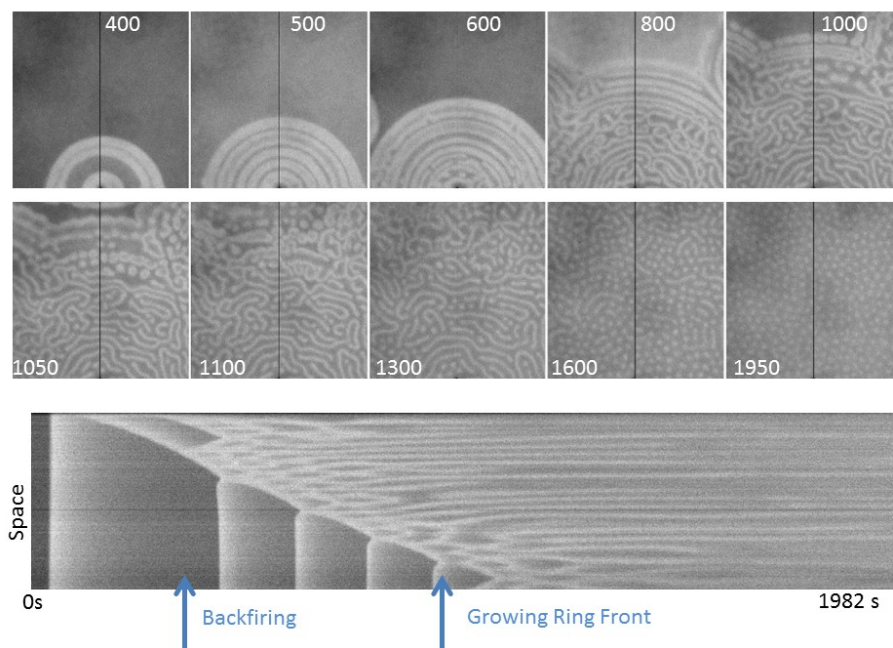
Figure 6.9: Settled Turing pattern with growing ring front. The upper sequence of images shows the development of the quasi-two dimensional spatial patterns. The lower space-time plot shows the development of the black line from the images over time. The arrows indicate the times when backfiring occurs and when the growing ring front occurs. Solution conditions: $[MA] = 0.25$ M, $[H_2SO_4] = 0.25$M, $[NaBrO_3]= 0.2$ M, $[ferroin]=10$mM, $\omega = 12.34$, $\phi_d = 0.40$. Images are 2.7mm x 2.7mm.
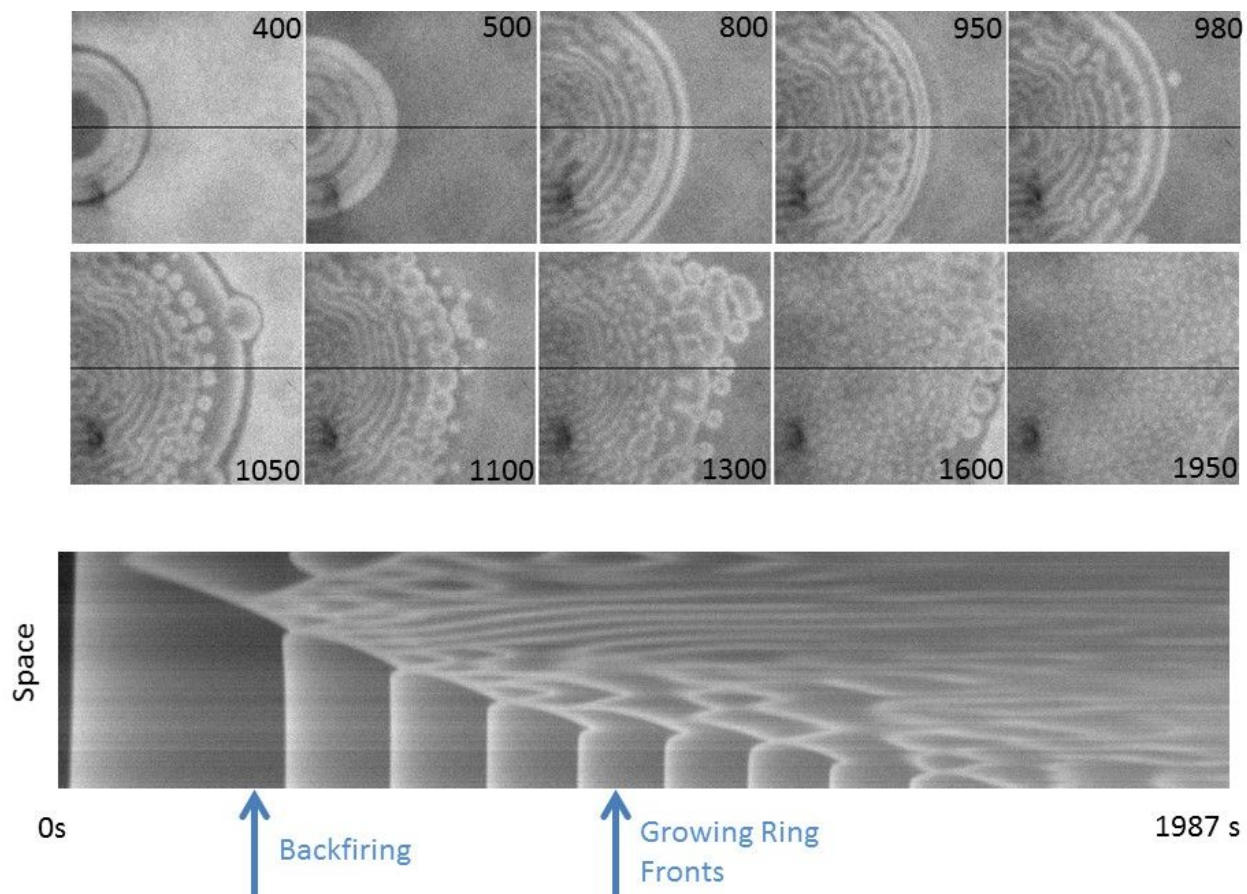
Figure 6.10: Settled Turing pattern with growing ring front. The upper sequence of images shows the development of the quasi-two dimensional spatial patterns. The lower space-time plot shows the development of the black line from the images over time. The arrows indicate the times when backfiring occurs and when the growing ring front occurs. Solution conditions: $[MA] = 0.25$ M, $[H_2SO_4] = 0.24$M, $NaBrO_3 = 0.2$ M, [ferroin]=10mM, $\omega = 12.34$, $\phi_d = 0.400$. Images are 2.7mm x 2.7mm.

Chapter 7

Mixed media, materials and modifications for an open reactor

As noted previously, the BZ-AOT system is a batch system, and while able to exhibit far-from-equilibrium behavior for more than ten hours [20] for certain patterns, the system eventually comes to equilibrium. It is more typical for patterns to last on the order of minutes to tens of minutes [84], making it unclear if pattern transitions occur because a pattern is a transient pattern or because of changes in the chemical conditions as the reaction ages. For patterns that last tens of minutes the former is typically assumed. The development of an open configuration for BZ-AOT would make it possible to determine which patterns are truly stable and allow access to study short-lived patterning regimes.

The development of a CFUR for BZ-AOT has been attempted previously by our group and others, however BZ-AOT is fundamentally different than CDIMA because it is a reverse microemulsion. Hydrogels, porous glass, and gel-impregnated membranes are materials that have been used in CDIMA CFURs to serve as the medium for pattern formation. We report our progress with membranes and microemulsion-based organogels as potential materials for

use in a CFUR system.

7.1 Membranes

Figures 7.1 and 7.2 show the formation of waves and Turing patterns in functionalized PVDF (Durapore polyvinylidene difluoride, (CH_2CF_2)n made by Millipore). Figure 7.1 has these membranes separated by a gap of BZ-AOT microemulsion. The patterning is slightly different in part of the solution, with modulating standing waves at the left membrane-solution interface and waves on the right solution-membrane interface. The Turing pattern wavelength is observed to decrease for the hydrophilic membrane. This could be due to the water droplets interacting with the membrane surface and therefore more often with each other (Figure 7.1). This would make sense, as Turing pattern wavelength decreases with increased PEO polymer concentration in the BZ-AOT [20].

These membranes were also used in conjuction with the bubble-free catalyst 1,4 cyclohexanedione. Figure 7.3 shows a pattern that appears as a slowly spreading circle of oxidation, but then the center fades, and lastly the edge fades.

7.2 Organogels

We have some preliminary results for a microemulsion-based organogel that is stable in the BZ-AOT reverse microemulsion. This gel is based on the preparation in Stouffer's Thesis[98], and the preparation is as described in the Methods section. Figure 7.4 shows a 1cm x 1cm x 1cm cube of gel that has been immersed in (left) for three hours and removed from (right) a BZ-AOT solution with CHD. The gel is transparent and has the same refractive index at the BZ-AOT, so the edges are not visually defined while immersed in solution. The air bubbles
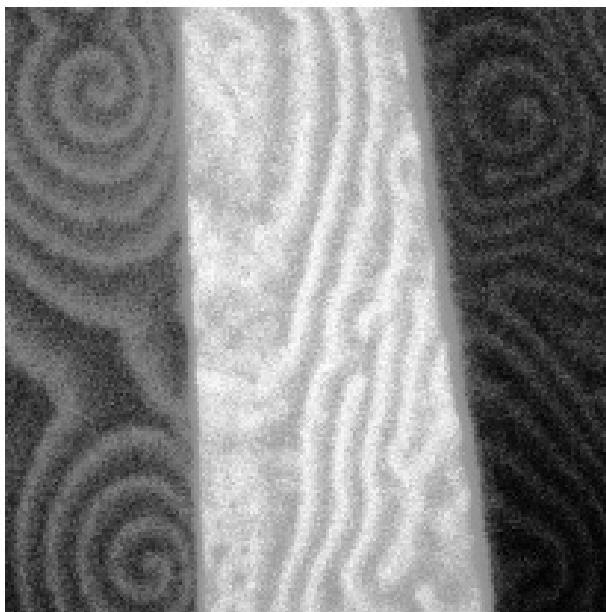
Figure 7.1: Spiral patterns and waves formed by the BZ-AOT microemulsion in two adjacent BZ-AOT saturated membranes separated by a gap of emulsion. The membranes are Durapore polyvinylidene difluoride (PVDF, $(CH_2CF_2)n$) (left: hydrophobic, 0.65 μm pore size, right: hydrophilic, 0.45 μm pore size)
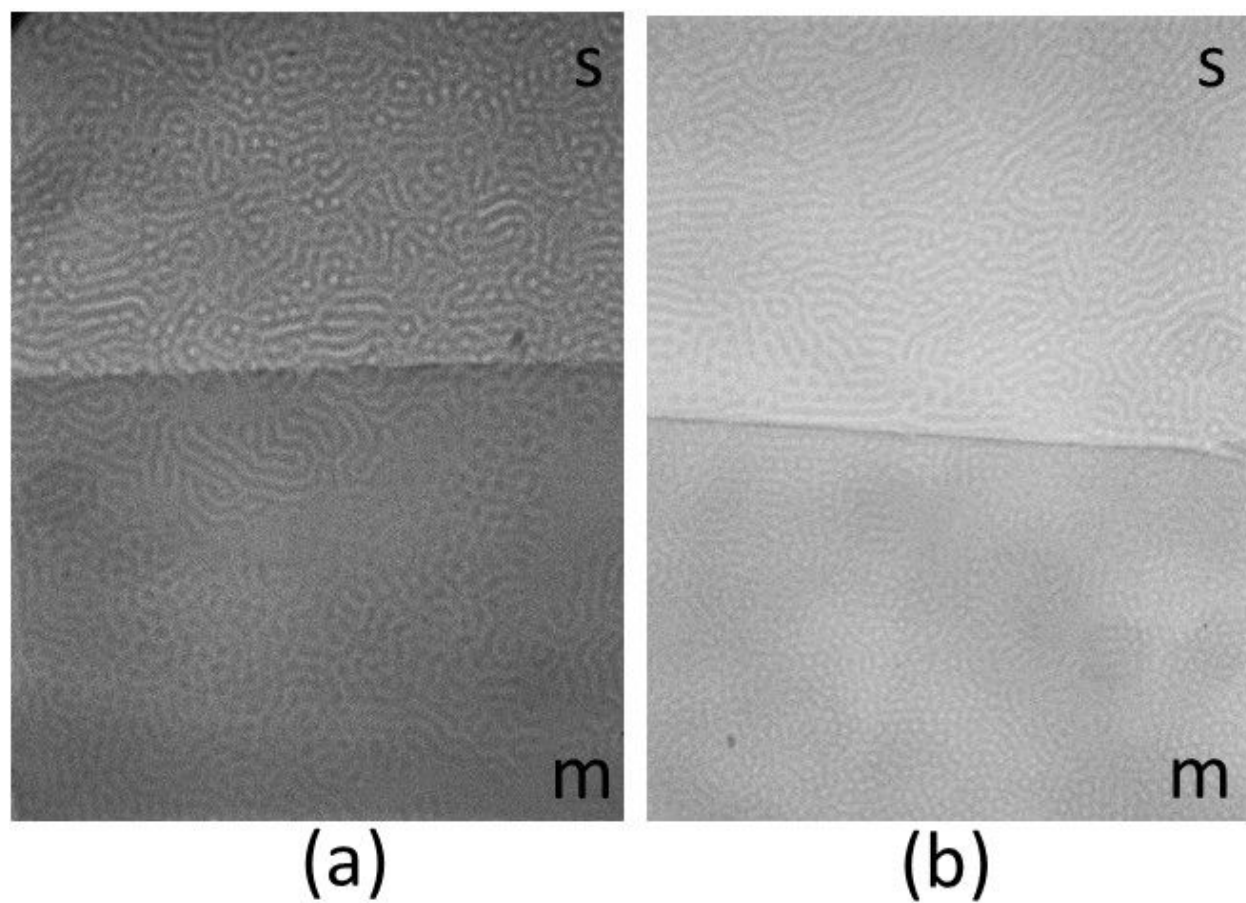
Figure 7.2: Turing patterns formed by the BZ-AOT microemulsion in solution (s) and in saturated functionalized PVDF membranes (m). Membrane specifications: (a) hydrophobic, 0.45 μm pore size, thickness 125 μm, (b) hydrophilic, 0.45 μm pore size, thickness 125 μm). Image size 2.96 x 3.95 mm
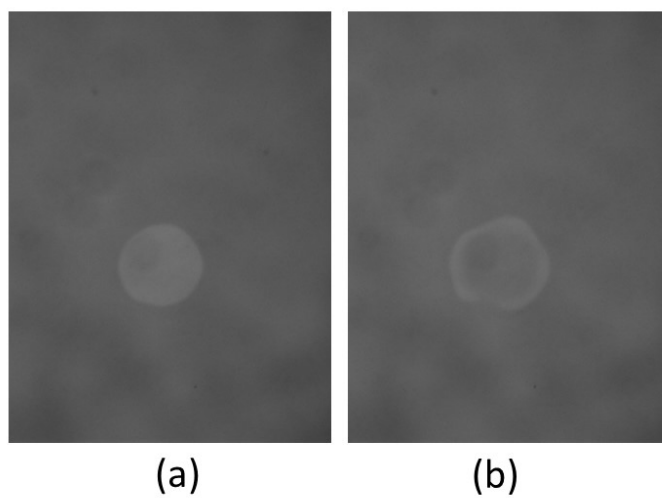
Figure 7.3: Fading ring in CHD BZ-AOT in PVDF membrane at times (a) 3942 and (b) 5639 s. Membrane specifications: (hydrophobic, 0.45 μm pore size). Chemical conditions: [CHD]=0.83 M, [H$_2$SO$_4$] = 0.2M, NaBrO$_3$= 0.08 M, [ferroin]=10mM, $\omega = 12.34$, $\phi_d = 0.58$

that are present in the gel can be seen. Removing the gel from the solution and patting it dry shows that the ferroin at least is absorbed in the gel.
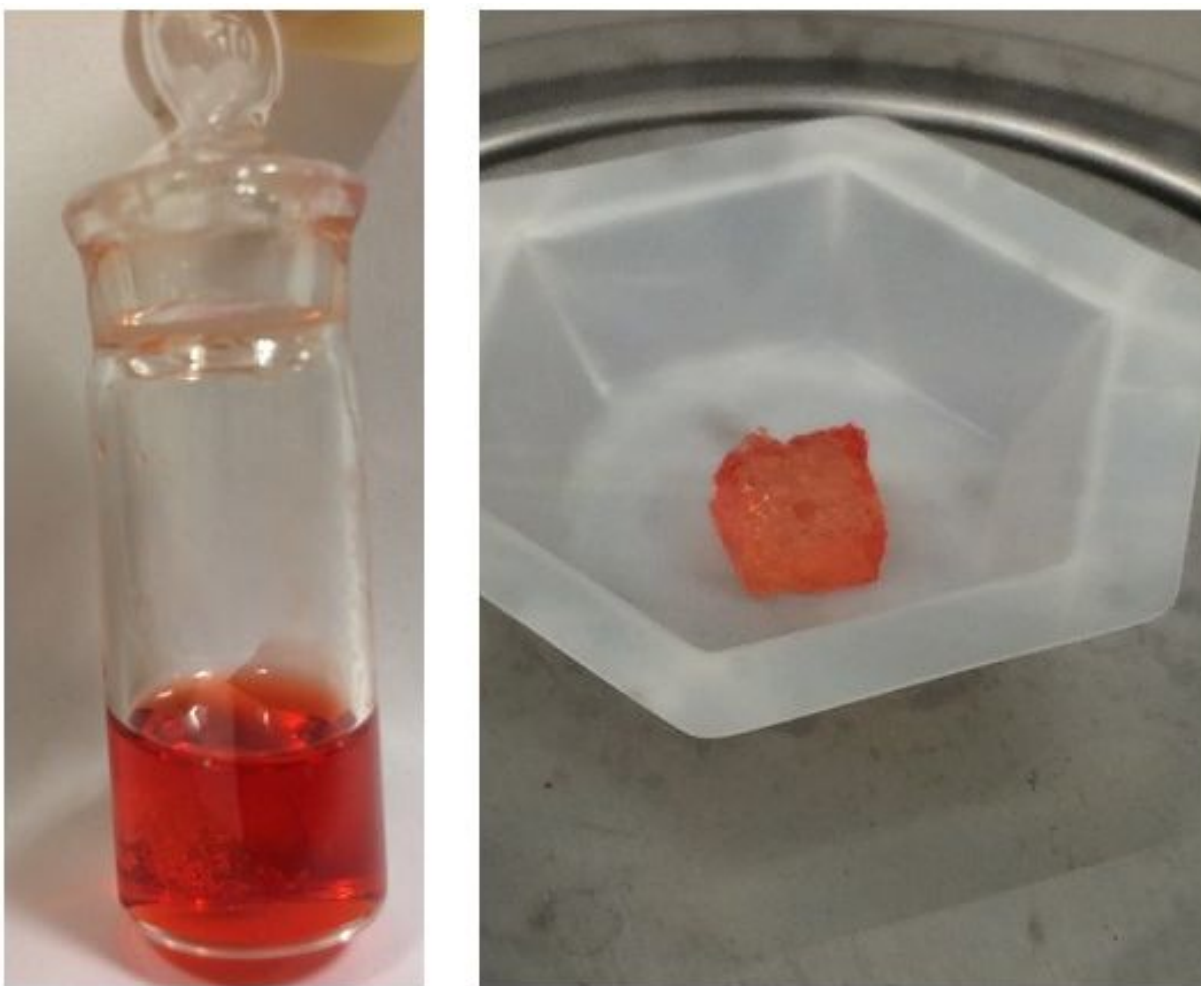
Figure 7.4: Gel immersed in BZ-AOT reactive microemulsion after 3 hours: (left) in solution, (right) removed from solution.

Chapter 8

Conclusion

This thesis has focused on extending pattern formation studies. This is done in (1) observations of new transition phenomena and (2) advancing new materials and methods to study pattern dynamics.

Historically, the first experimental observations of Turing pattern formation were decades after the observations of waves in nonlinear chemical systems [99] [12]. Certainly, that the patterns are ultimately stationary was the main thing at the time and still interesting, but so are their transition dynamics. The invasion of the steady state by Turing pattens was observed by Davies and colleagues in the De Kepper group [67] in the CDIMA system. In our pattern formation studies we have observed several different distinct Turing pattern invasion transition dynamics (Turing-Hopf invasion, settled Turing patterns, and growing rings) for Turing patterns invading a bulk oscillation domain. These pattern invasions are nearly indistinguishable until the first peak of the bulk oscillation. Then they develop in distinctly different ways. Settled Turing patterns and Turing-Hopf fronts are the most similar. In the Turing-Hopf front invasion, individual Turing stripes in the form of concentric rings are left behind as the Turing-Hopf front advances. The Turing-Hopf fronts are able to interfere with

each other as they advance and meet. The settled Turing patterns can have similar front dynamics with a front that resembles the Turing-Hopf front. The pattern centers are far more uneven than with the Turing-Hopf fronts, although this is reasonable as the pattern has much more freedom in settling than in individual rings. Growing rings can appear both at the onset of the pattern and at the front as the pattern is developing. We did not discuss at length that not all of the growing spots won their invasion against the bulk. In some cases, interaction during the bulk oscillation oxidation peak caused these growing spot to disappear. We suggested that the bulk oscillations have a vulnerability at certain points in their cycle to spatial perturbations that will grow. It would be interesting if the back-and-forth nature of invasion of Turing patterns observed numerically by Carballido and Berenstein (without a Turing-Hopf front) as well as Or-Guil (with a Turing-Hopf front) in this experimental system [78][91] could be related to the spots' growth and disappearance prior to the formation of the Turing patterns. The work in this thesis has advanced new materials and methods to study short-lived patterns and patterns transitions. Pattern to pattern transitions are of interest, as they offer warning for dynamical transitions that may occur in the system. In Chapter 3, we show a new route to increasing an individual Turing pattern's wavelength dynamically. This gives the opportunity to study pattern-to-pattern transitions for much longer wavelengths than could be achieved previously. This is done without imposing spatial forcing on the system, which has been shown to induce pattern formation that wouldn't occur in an unforced system[100].

The development of a CFUR is a longstanding challenge in the field and would allow for propositions that certain patterns are stable to be verified experimentally. It would also allow for controlled experiments on transient patterns and their transitions. In Chapter 7, we have obtained preliminary results for pattern formation in a reverse microemulsion system in a porous membrane. We've also shown the stability of a microemulsion-based organogel

in the microemulsion. These developments in materials are a significant step towards the development of an open reactor. The pattern that was discussed in Chapter 5 would benefit from study in a CFUR, particularly in the study of the death of the modulated standing waves. Bansagi noted the development of trigger waves and packet waves for the death of the standing waves[84], while ours become trigger spirals. Experiments to elucidate how the defects in the lattice of the standing wave lead to spiral formation would be a potential future direction.

Appendix A

Brusselator

A.1　Steady State

$$\frac{dX}{dt} = A + X^2 Y - BX - X \tag{A.1}$$

$$\frac{dY}{dt} = BX - X^2 Y \tag{A.2}$$

1) Find the steady state. We begin by setting the time derivatives to zero

$$\frac{dX}{dt} = 0 = A + X_{ss}^2 Y_{ss} - BX_{ss} - X_{ss} \tag{A.3}$$

$$\frac{dY}{dt} = 0 = BX_{ss} - X_{ss}^2 Y_{ss} \tag{A.4}$$

Then solve equation A.4 for BX_{ss}

$$0 = BX_{ss} - X_{ss}^2 Y_{ss} \tag{A.5}$$

$$BX_{ss} = X_{ss}^2 Y_{ss} \tag{A.6}$$

Plug this into Eq.A.3 and solve for X_{ss}

$$0 = A + BX_{ss} - BX_{ss} - X_{ss} \tag{A.7}$$

$$0 = A - X_{ss} \tag{A.8}$$

$$X_{ss} = A \tag{A.9}$$

Plug this into A.6

$$BA = A^2 Y_{ss} \tag{A.10}$$

$$Y_{ss} = B/A \tag{A.11}$$

A.2 Linear Stability Analysis

1) To solve for the Jacobian for Eqs.1.15 and 1.16.

$$J_{1,1} = \frac{\partial}{\partial X}\frac{dX}{dt} = 2XY - B - 1 \tag{A.12}$$

$$J_{1,2} = \frac{\partial}{\partial Y}\frac{dX}{dt} = +X^2 \tag{A.13}$$

$$J_{2,1} = \frac{\partial}{\partial X}\frac{dY}{dt} = B - 2XY \tag{A.14}$$

$$J_{2,2} = \frac{\partial}{\partial Y}\frac{dY}{dt} = -X^2 \tag{A.15}$$

The Jacobian is thus :

$$J = \begin{bmatrix} 2XY - B - 1 & X^2 \\ B - 2XY & -X^2 \end{bmatrix}$$

And when evaluated at the steady state it is: $J = \begin{bmatrix} 2(A)(B/A) - B - 1 & (A)^2 \\ B - 2(A)(B/A) & -(A)^2 \end{bmatrix} =$

$$
\begin{bmatrix} 2B - B - 1 & A^2 \\ B - 2B & -A^2 \end{bmatrix} = \begin{bmatrix} B - 1 & A^2 \\ -B & -A^2 \end{bmatrix}
$$

The determinant and the trace of this matrix are as follows:

$$
\det(J) = (-A^2)(B - 1) + B(A^2) \tag{A.16}
$$

$$
\det(J) = -A^2 B + A^2 + BA^2 \tag{A.17}
$$

$$
\det(J) = A^2 \tag{A.18}
$$

$$
\text{tr}(J) = B - 1 - A \tag{A.19}
$$

The characteristic equation is

$$
\lambda^2 - \text{tr}(J)\lambda + \det(J) = 0 \tag{A.20}
$$

where the λ are the eigenvalues. Solving this gives two solutions:

$$
\lambda_1 = \frac{\text{tr}(J)}{2} + \frac{\sqrt{\text{tr}(J)^2 - 4\det(J)}}{2} \tag{A.21}
$$

$$
\lambda_2 = \frac{\text{tr}(J)}{2} - \frac{\sqrt{\text{tr}(J)^2 - 4\det(J)}}{2} \tag{A.22}
$$

The real part of these eigenvalues changes sign when $\text{tr}(J){=}0$. It is positive when $B > 1 + A^2$. This is the onset of the Hopf bifurcation.

To find the onset of the Turing Bifurcation we need to satisfy two equations. The Linearized operator L is $L = J - k^2 D$ where $D = \begin{bmatrix} d & 0 \\ 0 & 1 \end{bmatrix}$ and $d = D_x/D_y$. That is:

$$L|_{X_{ss},Y_{ss}} = \begin{bmatrix} B - 1 - k^2 d & A^2 \\ -B & -A^2 - k^2 \end{bmatrix}$$

The first equation is $\det(L) = 0$

$$(B - 1 - d\,k^2)(-A^2 - k^2) - (-B)(A^2) = 0 \qquad (A.23)$$

$$(-A^2 B + A^2 + A^2 d\,k^2 - Bk^2 + k^2 + d\,k^4) + A^2 B = 0 \qquad (A.24)$$

$$A^2 + A^2 dk^2 - Bk^2 + k^2 + d\,k^4 = 0 \qquad (A.25)$$

$$A^2 + (A^2 d - B + 1)k^2 + d\,k^4 = 0 \qquad (A.26)$$

The second is $\frac{\partial \det(L)}{\partial k^2} = 0$

$$(A^2 d - B + 1) + 2d\,k^2 = 0 \qquad (A.27)$$

which makes the following true

$$(A^2 d - B + 1) = -2d\,k^2 \qquad (A.28)$$

Plugging in this into A.26 gives.

$$A^2 + (-2d\,k^2)k^2 + d\,k^4 = 0 \qquad (A.29)$$

$$A^2 - 2d\,k^4 + d\,k^4 = 0 \qquad (A.30)$$

$$A^2 - d\,k^4 = 0 \qquad (A.31)$$

$$d\,k^4 = A^2 \qquad (A.32)$$

$$k^4 = A^2/d \tag{A.33}$$

$$k^2 = A/d^{\frac{1}{2}} \tag{A.34}$$

Plugging this back into A.27:

$$(A^2 d - B + 1) + 2d(A/d^{\frac{1}{2}}) = 0 \tag{A.35}$$

$$A^2 d - B + 1 + 2Ad^{\frac{1}{2}} = 0 \tag{A.36}$$

$$1 + 2Ad^{\frac{1}{2}} + A^2 d = B \tag{A.37}$$

$$(1 + Ad^{\frac{1}{2}})^2 = B \tag{A.38}$$

Bibliography

[1] Richard J. Field, Endre Koros, and Richard M. Noyes. Oscillations in chemical systems. II. Thorough analysis of temporal oscillation in the bromate-cerium-malonic acid system. *Journal of the American Chemical Society*, 94(25):8649–8664, 12 1972.

[2] István Lengyel, Jing Li, Kenneth Kustin, and Irving R. Epstein. Rate Constants for Reactions between Iodine- and Chlorine-Containing Species: A Detailed Mechanism of the Chlorine Dioxide/Chlorite-Iodide Reaction †. *Journal of the American Chemical Society*, 118(15):3708–3719, 1996.

[3] Tapas K. De and Amarnath Maitra. Solution behaviour of Aerosol OT in non-polar solvents. *Advances in Colloid and Interface Science*, 59:95–193, 8 1995.

[4] James P. Keener and John J. Tyson. The Dynamics of Scroll Waves in Excitable Media. *SIAM Review*, 34(1):1–39, 1992.

[5] Ulrich Storb, Camilo Rodrigues Neto, Markus Bär, and Stefan C. Müller. A tomographic study of desynchronization and complex dynamics of scroll waves in an excitable chemical reaction with a gradient. *Phys. Chem. Chem. Phys.*, 5(11):2344–2353, 2003.

BIBLIOGRAPHY

[6] Zhilin Qu, Gang Hu, Alan Garfinkel, and James N. Weiss. Nonlinear and stochastic dynamics in the heart, 2014.

[7] Vladimir K Vanag and Irving R Epstein. Segmented spiral waves in a reaction-diffusion system. *Proceedings of the National Academy of Sciences of the United States of America*, 100(25):14635–8, 12 2003.

[8] A M Turing. The Chemical Basis of Morphogenesis. *Philosophical Transactions of the Royal Society B: Biological Sciences*, 237(641):37–72, 1952.

[9] William C. Bray. A PERIODIC REACTION IN HOMOGENEOUS SOLUTION AND ITS RELATION TO CATALYSIS. *Journal of the American Chemical Society*, 43(6):1262–1267, 6 1921.

[10] B.P. Belousov. full-text. *Collection of Short Papers on Radiation Medicine*, page 145, 1955.

[11] Anatol M. Zhabotinsky. A history of chemical oscillations and waves. *Chaos: An Interdisciplinary Journal of Nonlinear Science*, 1(4):379–386, 12 1991.

[12] V Castets, E Dulos, J Boissonade, and De Kepper P. Experimental evidence of a sustained standing Turing-type nonequilibrium chemical pattern. *Physical Review Letters*, 64(24):2953–2956, 1990.

[13] L. Kuhnert. Chemische Strukturbildung in festen Gelen auf der Basis der Belousov-?abotinskij-Reaktion. *Naturwissenschaften*, 70(9):464–466, 9 1983.

[14] Qi Ouyang, Rusheng Li, Ge Li, and Harry L. Swinney. Dependence of Turing pattern wavelength on diffusion rate. *The Journal of Chemical Physics*, 102(6):2551, 2 1995.

[15] Kouichi Asakura, Ryo Konishi, Tomomi Nakatani, Takaya Nakano, and Masazumi Ka-mata. Turing pattern formation by the CIMA reaction in a chemical system consisting of quaternary alkyl ammonium cationic groups. *The journal of physical chemistry. B*, 115(14):3959–63, 2011.

[16] D. Balasubramanian and G. A. Rodley. Incorporation of chemical oscillators into organized surfactant assemblies. *Journal of Physical Chemistry*, 92(21):5995–5998, 1988.

[17] Jerzy Maselko and Kenneth Showalter. Chemical waves on spherical surfaces. *Nature*, 339(6226):609–611, 6 1989.

[18] Ryo Yoshida, Hisao Ichijo, Toshikatsu Hakuta, and Tomohiko Yamaguchi. Self-oscillating swelling and deswelling of polymer gels. *Macromolecular Rapid Communications*, 16(4):305–310, 4 1995.

[19] Daniel Cuiñas, Igal Berenstein, Jorge Carballido-Landeira, and Alberto P. Muñuzuri. Transition from traveling to standing waves as a function of frequency in a reaction-diffusion system. *Journal of Chemical Physics*, 128(24):244907, 6 2008.

[20] Jorge Carballido-Landeira, Igal Berenstein, Pablo Taboada, Victor Mosquera, Vladimir K Vanag, Irving R Epstein, Vicente Pérez-Villar, and Alberto P Muñuzuri. Long-lasting dashed waves in a reactive microemulsion. *Physical chemistry chemical physics : PCCP*, 10(8):1094–6, 2 2008.

[21] Arthur T. Winfree. ROTATING CHEMICAL REACTIONS, 1974.

[22] Vladimir K. Vanag and Dmitrii V. Boulanov. Behavior of the Belousov-Zhabotinskii

Oscillator in Reverse Micelles of AOT in Octane. *The Journal of Physical Chemistry*, 98(5):1449–1453, 2 1994.

[23] D. Balasubramanian and G. A. Rodley. Incorporation of chemical oscillators into organized surfactant assemblies. *The Journal of Physical Chemistry*, 92(21):5995–5998, 10 1988.

[24] I. Gonda and G. A. Rodley. Oscillatory behavior of a Belousov-Zhabotinskii reverse micelle system. *Journal of Physical Chemistry*, 94(4):1516–1519, 1990.

[25] V K Vanag and I R Epstein. Inwardly rotating spiral waves in a reaction-diffusion system. *Science (New York, N.Y.)*, 294(5543):835–7, 10 2001.

[26] Alexander A Cherkashin, Vladimir K Vanag, and Irving R Epstein. Discontinuously propagating waves in the bathoferroin-catalyzed Belousov–Zhabotinsky reaction incorporated into a microemulsion.

[27] V K Vanag and I R Epstein. Pattern formation in a tunable medium: the Belousov-Zhabotinsky reaction in an aerosol OT microemulsion. *Physical Review Letters*, 87(22):228301, 2001.

[28] T. Yamaguchi, L. Kuhnert, Z. Nagy-Ungvarai, S. C. Mueller, and B. Hess. Gel systems for the Belousov-Zhabotinskii reaction. *The Journal of Physical Chemistry*, 95(15):5831–5837, 7 1991.

[29] Susan J Law and Melanie M Britton. Sizing of reverse micelles in microemulsions using NMR measurements of diffusion. *Langmuir : the ACS journal of surfaces and colloids*, 28(32):11699–706, 8 2012.

[30] Jorge Carballido-Landeira, Vladimir K Vanag, and Irving R Epstein. Patterns in the Belousov–Zhabotinsky reaction in water-in-oil microemulsion induced by a temperature gradient. 2010.

[31] Jorge Carballido-Landeira, Pablo Taboada, and Alberto P. Muñuzuri. Nanoscale changes induce microscale effects in Turing patterns. *Physical Chemistry Chemical Physics*, 13(10):4596, 2011.

[32] Patricia D??hmlow, Vladimir K. Vanag, and Stefan C. M??ller. Effect of solvents on the pattern formation in a Belousov-Zhabotinsky reaction embedded into a microemulsion. *Physical Review E - Statistical, Nonlinear, and Soft Matter Physics*, 89(1):1–5, 2014.

[33] Georg Brauer, editor. *Handbook of Preparative Inorganic Chemistry*. New York, 2nd ed. edition, 1963.

[34] Tamás Bánsági, Vladimir K Vanag, and Irving R Epstein. Tomography of reaction-diffusion microemulsions reveals three-dimensional Turing patterns. *Science*, 331(6022):1309–1312, 2011.

[35] Toshio Sekimura, Chandrasekhar Venkataraman, and Anotida Madzvamuse. A Model for Selection of Eyespots on Butterfly Wings. *PloS one*, 10(11):e0141434, 1 2015.

[36] Motoomi Yamaguchi, Eiichi Yoshimoto, and Shigeru Kondo. Pattern regulation in the stripe of zebrafish suggests an underlying dynamic and autonomous mechanism. *Proceedings of the National Academy of Sciences of the United States of America*, 104(12):4790–3, 3 2007.

[37] D Bullara and Y De Decker. Pigment cell movement is not required for generation of Turing patterns in zebrafish skin. *Nature Communications*, 6:6971, 1 2015.

[38] Rushikesh Sheth, Luciano Marcon, M Félix Bastida, Marisa Junco, Laura Quintana, Randall Dahn, Marie Kmita, James Sharpe, and Maria A Ros. Hox genes regulate digit patterning by controlling the wavelength of a Turing-type mechanism. *Science (New York, N.Y.)*, 338(6113):1476–80, 12 2012.

[39] R. HillerisLambers, M.G. Rietkerk, F. van den Bosch, H.H.T. Prins, and H. de Kroon. Vegetation pattern formation in semi-arid grazing systems. *Ecology*, 82:50–61, 2001.

[40] Ehud Meron, Erez Gilad, Jost von Hardenberg, Moshe Shachak, and Yair Zarmi. Vegetation patterns along a rainfall gradient. *Chaos, Solitons & Fractals*, 19(2):367–376, 1 2004.

[41] Marten Scheffer, Jordi Bascompte, William A Brock, Victor Brovkin, Stephen R Carpenter, Vasilis Dakos, Hermann Held, Egbert H van Nes, Max Rietkerk, and George Sugihara. Early-warning signals for critical transitions. *Nature*, 461(7260):53–9, 9 2009.

[42] Koen Siteur, Eric Siero, Maarten B. Eppinga, Jens D.M. Rademacher, Arjen Doelman, and Max Rietkerk. Beyond Turing: The response of patterned ecosystems to environmental change. *Ecological Complexity*, 20:81–96, 12 2014.

[43] William F Laurance, Henrique E M Nascimento, Susan G Laurance, Ana Andrade, Robert M Ewers, Kyle E Harms, Regina C C Luizão, and José E Ribeiro. Habitat fragmentation, variable edge effects, and the landscape-divergence hypothesis. *PloS one*, 2(10):e1017, 1 2007.

[44] Ángel de Frutos, Teresa Navarro, Yolanda Pueyo, and Concepción L Alados. Inferring resilience to fragmentation-induced changes in plant communities in a semi-arid Mediterranean ecosystem. *PloS one*, 10(3):e0118837, 1 2015.

[45] John A. Endler. Natural Selection on Color Patterns in Poecilia reticulata on JSTOR. *Evolution*, 34(1):76–91, 1980.

[46] Tim Caro, Amanda Izzo, Robert C Reiner, Hannah Walker, and Theodore Stankowich. The function of zebra stripes. *Nature communications*, 5:3535, 1 2014.

[47] I Lengyel, S Kádár, and I R Epstein. Transient turing structures in a gradient-free closed system. *Science (New York, N.Y.)*, 259(5094):493–5, 1 1993.

[48] B. Rudovics, E. Barillot, P. W. Davies, E. Dulos, J. Boissonade, and P. De Kepper. Experimental Studies and Quantitative Modeling of Turing Patterns in the (Chlorine Dioxide, Iodine, Malonic Acid) Reaction. *The Journal of Physical Chemistry A*, 103(12):1790–1800, 3 1999.

[49] Zoltan Noszticzius, Qi Ouyang, William D. McCormick, and Harry L. Swinney. Effect of Turing pattern indicators on CIMA oscillators. *The Journal of Physical Chemistry*, 96(15):6302–6307, 7 1992.

[50] David G Míguez, Milos Dolnik, Alberto P Muñuzuri, and Lorenz Kramer. Effect of axial growth on Turing pattern formation. *Physical Review Letters*, 96(4):048304, 2 2006.

[51] Oscar Valdes-Aguilera, Donald W. Boyd, Irving R. Epstein, and Kenneth Kustin. Systematic design of chemical oscillators. Part 35. Kinetics and mechanism of the reaction between chlorine(III) and bromide ion. *The Journal of Physical Chemistry*, 90(25):6702–6708, 12 1986.

[52] Reuben H. Simoyi. Autocatalytic chlorite-bromide reaction. *The Journal of Physical Chemistry*, 89(16):3570–3574, 8 1985.

[53] Mohamed Alamgir and Irving R. Epstein. Systematic design of chemical oscillators. Part 31. New chlorite oscillators: chlorite-bromide and chlorite-thiocyanate in a CSTR. *The Journal of Physical Chemistry*, 89(17):3611–3614, 1985.

[54] Zsuzsanna Tóth and István Fábián. Kinetics and mechanism of the initial phase of the bromine- chlorite ion reaction in aqueous solution. *Inorganic Chemistry*, 39(20):4608–4614, 2000.

[55] C C Hong and W H Rapson. Analyses of chlorine dioxide,chlorous acid, chlorite, Chlorate , and Chloride in Composite Mixtures. *Canadian Journal of Chemistry*, 46:2061–2064, 1968.

[56] Guy Schmitz and Henri Rooze. Mecanisme des reactions du chlorite et du dioxyde de chlore. 5. Cinetique de la reaction chlorite-bromure. *Canadian Journal of Chemistry*, 65:497–501, 1987.

[57] Guy Schmitz and Henri Rooze. Mecanisme des reactions du chlorite et du dioxyde de chlore. 2. Cinetique des reactions du chlorite en presence d'ortho-tolidine. *Canadian Journal of Chemistry*, 62:2231–2234, 1984.

[58] Jeffrey S. Nicoson and Dale W. Margerum. Kinetics and Mechanisms of Aqueous Chlorine Reactions with Chlorite Ion in the Presence of Chloride Ion and Acetic Acid/Acetate Buffer. *Inorganic Chemistry*, 41(2):342–347, 1 2002.

[59] Balázs Kormányos, István Nagypál, Gábor Peintler, and Attila K Horváth. Effect of chloride ion on the kinetics and mechanism of the reaction between chlorite ion and hypochlorous acid. *Inorganic chemistry*, 47(17):7914–20, 9 2008.

[60] I Lengyel and I R Epstein. Modeling of turing structures in the chlorite–iodide–malonic Acid–starch reaction system. *Science (New York, N.Y.)*, 251(4994):650–2, 2 1991.

[61] Scott J. McIndoe and Dennis G. Tuck. Studies of polyhalide ions in aqueous and non-aqueous solution by electrospray mass spectrometry. *Dalton Transactions*, (2):244–248, 1 2003.

[62] Lars Fride Olsson. Halide-exchange reactions of mixed chloro-bromo-iodo trihalides. 1. Equilibria in the chloro-iodo system. *Inorganic Chemistry*, 24(9):1398–1405, 4 1985.

[63] Robert C. Troy, Mark D. Kelley, Julius C. Nagy, and Dale W. Margerum. Non-metal redox kinetics: iodine monobromide reaction with iodide ion and the hydrolysis of IBr. *Inorganic Chemistry*, 30(25):4838–4845, 12 1991.

[64] Derek G. Leaist. Ternary diffusion with charged-complex formation in aqueous I2+NaI and I2+KI solutions. *Journal of Solution Chemistry*, 17(4):359–369, 4 1988.

[65] Vladimir K Vanag and Irving R Epstein. Cross-diffusion and pattern formation in reaction-diffusion systems. *Physical chemistry chemical physics : PCCP*, 11(6):897–912, 2 2009.

[66] Alexander Schmidt, Theodoros Kasimatis, Johanne Hizanidis, Astero Provata, and Philipp Hövel. Chimera patterns in two-dimensional networks of coupled neurons. *Physical Review E*, 95(3), 2017.

[67] P. W. Davies, P. Blanchedeau, E. Dulos, and P. De Kepper. Dividing Blobs, Chemical Flowers, and Patterned Islands in a Reaction-Diffusion System. *The Journal of Physical Chemistry A*, 102(43):8236–8244, 10 1998.

[68] Xiaosong Tang, Yongli Song, and Tonghua Zhang. Turing–Hopf bifurcation analysis of a predator–prey model with herd behavior and cross-diffusion. *Nonlinear Dynamics*, 86(1):73–89, 2016.

[69] Moira L. Steyn-Ross, D. A. Steyn-Ross, and J. W. Sleigh. Interacting Turing-Hopf Instabilities Drive Symmetry-Breaking Transitions in a Mean-Field Model of the Cortex: A Mechanism for the Slow Oscillation. *Physical Review X*, 3(2):021005, 5 2013.

[70] M. Ouali, S. Coulibaly, M. Taki, and M. Tlidi. Extended and localized Hopf-Turing mixed-mode in non-instantaneous Kerr cavities. *Optics Express*, 25(5):4714, 3 2017.

[71] Maya Mincheva and Marc R. Roussel. Turing-Hopf instability in biochemical reaction networks arising from pairs of subnetworks. *Mathematical Biosciences*, 240(1):1–11, 11 2012.

[72] Debora Laacitignola, Benedetto Bozzini, and Ivonne Sgura. Spatio-temporal organization in a morphochemical electrodeposition model: Hopf and Turing instabilities and their interplay. *European Journal of Applied Mathematics*, 26(02):143–173, 4 2015.

[73] S. Alonso, D. G. Míguez, and F. Sagués. Differential susceptibility to noise of mixed Turing and Hopf modes in a photosensitive chemical medium. *Europhysics Letters*, 81(3):30006, 2008.

[74] Vladimir K. Vanag and Irving R. Epstein. Stationary and Oscillatory Localized Patterns, and Subcritical Bifurcations. *Physical Review Letters*, 92(12):128301, 2004.

[75] J.-J. Perraud, A. De Wit, E. Dulos, P. De Kepper, G. Dewel, and P. Borckmans. One-dimensional "spirals": Novel asynchronous chemical wave sources. *Physical Review Letters*, 71(8):1272–1275, 8 1993.

[76] H. Willebrand, K. Matthiessen, F.-J. Niedernostheide, R. Dohmen, and H.-G. Purwins. Experimental Observation of Simultaneously Existing Moving and Standing Patterns in a Gas-Discharge System. *Contributions to Plasma Physics*, 32(2):57–68, 1992.

[77] G. Heidemann, M. Bode, and H.-G. Purwins. Fronts between Hopf- and Turing-type domains in a two-component reaction-diffusion system. *Physics Letters A*, 177(3):225–230, 1993.

[78] M Or-Guil and M Bode. Propagation of Turing–Hopf fronts. *Physica A*, 249(1-4):174–178, 1 1998.

[79] Igal Berenstein and Jorge Carballido-Landeira. Back and forth invasion in the interaction of Turing and Hopf domains in a reactive microemulsion system. *RSC Advances*, 6(62):56867–56873, 2016.

[80] Sergio Alonso and Francesc Sagués. Noise-reversed stability of Turing patterns versus Hopf oscillations near codimension-two conditions. *Physical Review E*, 80(3):035203, 9 2009.

[81] Patricia Dähmlow, Vladimir K Vanag, and Stefan C Müller. Effect of solvents on the pattern formation in a Belousov-Zhabotinsky reaction embedded into a microemulsion. *Physical Review E*, 89(1):010902, 1 2014.

[82] Giulio Vandin, Davide Marenduzzo, Andrew B. Goryachev, and Enzo Orlandini. Curvature-driven positioning of Turing patterns in phase-separating curved membranes. *Soft Matter*, 12(17):3888–3896, 2016.

[83] Akiko Kaminaga, Vladimir K Vanag, and Irving R Epstein. Wavelength halving in

a transition between standing waves and traveling waves. *Physical Review Letters*, 95(5):058302, 2005.

[84] Tamás Bánsági, Vladimir K. Vanag, and Irving R. Epstein. Two- and three-dimensional standing waves in a reaction-diffusion system. *Physical Review E*, 86(4):045202, 2012.

[85] Vladimir K Vanag and Irving R Epstein. Subcritical wave instability in reaction-diffusion systems. *Journal of Chemical Physics*, 121(2):890–894, 2004.

[86] B Peña and M Bestehorn. THE EUROPEAN PHYSICAL JOURNAL Two-dimensional wave patterns near a Hopf–Wave interaction in a chemical model. *Eur. Phys. J. Special Topics*, 146:301–311, 2007.

[87] B. Peña, C. Pérez-García, and M. Bestehorn. MODULATED STANDING WAVES RESULTING FROM A HOPF–WAVE INTERACTION IN A CHEMICAL MODEL. *International Journal of Bifurcation and Chaos*, 14(11):3899–3907, 11 2004.

[88] Alexander von Oertzen, Harm H. Rotermund, Alexander S. Mikhailov, and Gerhard Ertl. Standing Wave Patterns in the CO Oxidation Reaction on a Pt(110) Surface: Experiments and Modeling. *The Journal of Physical Chemistry B*, 104(14):3155–3178, 2000.

[89] Igal Berenstein. Standing wave-like patterns in the Gray-Scott model. *Chaos: An Interdisciplinary Journal of Nonlinear Science*, 25(6):064301, 2015.

[90] Tamás Bánsági, Vladimir K Vanag, and Irving R Epstein. Tomography of reaction-diffusion microemulsions reveals three-dimensional Turing patterns. *Science*, 331(6022):1309–12, 2011.

BIBLIOGRAPHY

[91] Igal Berenstein and Jorge Carballido-Landeira. Back and forth invasion in the interaction of Turing and Hopf domains in a reactive microemulsion system. *RSC Advances*, 6(62):56867–56873, 2016.

[92] Lingfa Yang, Milos Dolnik, Anatol M. Zhabotinsky, and Irving R. Epstein. Pattern formation arising from interactions between Turing and wave instabilities. *The Journal of Chemical Physics*, 117(15):7259, 2002.

[93] Igal Berenstein. Distinguishing similar patterns with different underlying instabilities: Effect of advection on systems with Hopf, Turing-Hopf, and wave instabilities. *Chaos: An Interdisciplinary Journal of Nonlinear Science*, 22(4):043109, 12 2012.

[94] Vladimir K. Vanag and Irving R. Epstein. Dash Waves in a Reaction-Diffusion System. *Physical Review Letters*, 90(9):4, 2003.

[95] Lingfa Yang, Igal Berenstein, and Irving R Epstein. Segmented waves from a spatiotemporal transverse wave instability. *Physical Review Letters*, 95(3), 2005.

[96] Andrey Polezhaev and Maria Borina. On the Mechanisms for Formation of Segmented Waves in Active Media. pages 341–348. Springer, Cham, 2014.

[97] Chaiya Luengviriya, Stefan C. Müller, and Marcus J. B. Hauser. Reorientation of scroll rings in an advective field. *Physical Review E*, 77(1):015201, 1 2008.

[98] Melissa Stouffer. A STUDY OF ORGANOGELS AND THEIR SOLUTE INTERACTIONS.

[99] A T Winfree. Spiral waves of chemical activity. *Science (New York, N.Y.)*, 175(4022):634–6, 2 1972.

[100] Yair Mau, Aric Hagberg, and Ehud Meron. Spatial Periodic Forcing Can Displace Patterns It Is Intended to Control. *Physical Review Letters*, 109(3):034102, 7 2012.